

Observation of the Non-uniform Poloidal Flow of Impurity Ion
on Magnetic Surfaces using Bidirectional Charge Exchange
Spectroscopy in CHS

Shin Nishimura

Doctor of Science

Department of Fusion Science
School of Mathematical and Physical Science
The Graduate University for Advanced Studies

1997

Abstract

The radial electric fields in magnetically confined toroidal plasmas are considered to play an important role in plasma confinements. For example, they change the neoclassical ripple loss in the low collisionality regime in helical devices, and they are considered to be the important parameter to determine the L/H transition and the anomalous transport characteristics of L/H-modes in tokamak plasmas. Therefore many efforts to study the radial electric fields experimentally have been performed. One method for this study is the spectroscopic measurements of the rotations of impurity ions. However, toroidal effects on the plasma rotations have never been studied experimentally. The coupling of toroidal and poloidal rotations caused by the toroidal effect to satisfy the poloidal flow conservation condition is the most important basis of neoclassical transport theory and is also important for understanding the supersonic (with $M_p \sim 1$ where M_p is the poloidal Mach number) plasma flows in tokamak H-mode plasmas. Therefore many related theoretical studies have been made.

To study this problem experimentally is to compare poloidal flux on the inside and outside of the magnetic surfaces. In the poloidal rotation measurements in many tokamaks, the poloidal rotation velocities only in the outsides were measured, since it is difficult to install the observation chords viewing vertically the insides of the torus. Another severe difficulty is the calibration of mechanical wavelength offset($\sim 0.5 \text{ \AA}$) of spectrometers with the accuracy for the plasma rotation measurements. The study of the inside/outside asymmetry of poloidal rotation velocity requires the accuracy of absolute wavelength of $\sim 0.01 \text{ \AA}$. To measure the absolute value of the rotation velocity canceling this offset, it needs the observation along opposite viewing directions. In past plasma rotation measurements using the observation from one direction only, some

assumptions or approximations about the plasma rotation velocity profiles were used. For example, the average of the poloidal rotation velocities in the inside and the outside was used as poloidal rotation 'velocity' in Heliotron E.

In the present work, I have carried out the measurement of the profiles of the poloidal rotation velocity, the temperature and the density of impurity ions using bidirectional charge exchange spectroscopy(CXS) in the Compact Helical System(CHS). For the purpose mentioned above, this measurement system uses two fiber arrays to view vertically the beam line from up and down sides simultaneously at one vertically elongated section. In Heliotron/Torsatron devices as like CHS, the strong parallel viscosity reduces the parallel ion flow velocity which is necessary for incompressible flow conservation when the perpendicular ion flow exists in low aspect ratio tori. This damping is strong in peripheral region where the helical ripple becomes large. However, the poloidal rotation of impurity ions mainly driven by radial electric field determined by the ambipolar condition of the electron and ion fluxes is also large in this peripheral region. Therefore the compensation of the asymmetry of inside and outside perpendicular flows by the parallel flows becomes difficult in this region. When the electrostatic potential is the surface quantity and the poloidal rotation of ions is mainly the $E \times B$ drift, the flow, especially of the impurity ions having low pressure, should be compressible. Otherwise the electrostatic potential is not the surface quantity or the poloidal rotation of impurity ions is not $E \times B$ drift. Investigating this problem is easier in low aspect ratio devices. Therefore this measurement in CHS with the lowest aspect ratio $R_0/a=5$ in helical devices will give the new information about the plasma rotations.

The preliminary measurements of plasma rotations using this system clarified some technical problems in multi-channel CXS. The most important problem was the apparent wavelength shift caused by the spectral fine structure of hydrogen-like ions used in CXS. This structure

is the red-side/blue-side asymmetric splitting of the lines due to a relativistic effect and thus cause the red-side/blue-side asymmetry of the Doppler broadened spectral profile. Because of this asymmetry, the wavelength given by single Gaussian least square fitting shows the apparent shifts which depends on Doppler widths. The observed apparent shifts of CVI lines, not due to plasma rotation, in the plasma peripheral region ($T_i \sim 100\text{eV}$) and in the after-glow recombining phase ($T_i \sim 30\text{eV}$) are always red-shifts regardless the direction of plasma rotation. The magnitude corresponds to the velocity error of a few km/s. This direction and magnitude are consistent with the calculation using the collisional l-mixing model. This value is not negligible in CHS plasmas, and thus should be corrected.

The density profile of the fully ionized impurity ions can be measured using the intensity of the charge exchange spectral lines. For this purpose, the initial beam density profile without attenuation was also measured in the torus using H_α from the beam. The measured density profile was a broad and inside shifted profile compared with the calculated one. This result means the possibility to measure the parameters on inside of the torus with CXS. However, the calculation of the beam attenuation required that the average electron densities should be less than $2 \times 10^{13}\text{cm}^{-3}$ to avoid the ambiguity of beam attenuation calculation and the degradation of signal level on the inside.

The measurements of the asymmetry of the poloidal flux of fully ionized carbon ions on the inside and outside of the torus were carried out for the magnetic surface configurations with different magnetic axis positions. In the inward shifted configurations, the gradients of surface function ($d\Psi/dR$) on the inside and outside of the section are almost symmetric. It becomes asymmetric in the outward shifted configuration and the strength of the radial electric field will become asymmetric in these configuration.

The asymmetry of the Doppler shifts of the CVI line($\Delta n=8-7, \lambda$

$\approx 5290 \text{ \AA}$) on the inside and outside of the torus was successfully measured. In the outward shifted configuration, the electrostatic potential calculated from this velocity using the momentum balance equation is the surface quantity. The measured density of impurity ions have a hollow profile and is higher on the inside of the magnetic surfaces compared with that on the outside. This inside/outside asymmetry of the density profile can be explained by the poloidal flow conservation on both sides under the damping of toroidal rotation.

In the inward shifted configuration, the density profile is a flat or peaking profile and the inside/outside asymmetry is not clear. The quantitative comparison of the electrostatic potential and the poloidal flow on both sides is difficult in the inward shifted configurations because of the intense background radiation at the inside of the magnetic axis. It causes the degradation of signal/noise ratio of spectrum after subtracting background spectrum. However, this change in the density asymmetry is consistent with the past measurement of the toroidal rotation damping and suggests the poloidal rotation accompanying the inside/outside asymmetric toroidal flow. Therefore the measurement of inside/outside asymmetry of the toroidal rotation velocity is an interesting future theme.

Acknowledgements

The author wishes to express his sincere gratitude to Dr. Katsumi Ida for the useful suggestions and the continuous advise on this work.

The author would like to thank Prof. Shigeru Sudo and the Director-General Atsuo Iiyoshi of National Institute for Fusion Science for the giving him the chance to study in this institute and the continuous encouragement. The author's this gratitude is extended to Prof. Hideki Zushi and Prof. Katsumi Kondo in Kyoto University and Mr. Ikujiro Nakano and Mr. Yoshihiko Miyano in Hitachi,Ltd.

The author acknowledges the experimental supports and the suggestions by Prof. Keisuke Matsuoka, Prof. Shouichi Okamura and the all members of CHS group. He could not do this work without the NBI operation and the information about NBI system by Dr. Masaki Osakabe, the electron temperature and density measurements by Dr. Takashi Minami and Dr. Kenji Tanaka, and the data acquisition system operation by Mr. Chihiro Takahashi. He must send grateful thank to them. The author also thanks Dr. Akihide Fujisawa for providing the magnetic field calculation code and the useful discussions on this work. The information about the local island diverter (LID) experiments from Dr. Tomohiro Morisaki and the information about the soft X-ray measurements from Dr. Satoshi Ohdachi are also appreciated.

The author thanks the members of R&D division, especially Dr. Keiichi Hirano, Dr. Masayoshi Tanaka, Dr. Mamiko Sasao, Dr. Hiroyuki Sakaue, and Dr. Shin-ichiro Kado for the useful discussions on this work and their continuous encouragement. He wishes to express his gratitude also to Prof. Kimitaka Itoh and Dr. Heiji Sanuki for the advise and the encouragement, and thanks Prof. Masami Fujiwara, Prof. Osamu Motojima, Prof. Tsutomu Kuroda, Prof. Yasuji Hamada and Prof. Toshio Watari for the encouragement.

The author was partially supported by the fusion science association. The author further thanks his seniors and colleagues in Kyoto University, Hitachi,Ltd. and Graduated University for Advanced Studies, especially Dr. Nobuhiro Nishino, Dr. Ryukichi Takahashi, Dr. Yukio Nakano, Dr. Yuuji Nakamura, Dr. Hideo Sugama, Dr. Masatoshi Yagi, Dr. Mitsutaka Isobe and Dr. Seishu Lee for their advise, supports and encouragement.

The author dedicates this thesis to the memory of his grandmothers Yae Nishimura and Fumi Tanaka.

Contents

Abstracts

Acknowledgements

Chapter 1. Introduction

- 1.1 Overview
- 1.2 Compact Helical System
- 1.3 Outline of Thesis

Chapter 2. Charge Exchange Spectroscopy System in CHS

- 2.1 Diagnostics Principles
- 2.2 Bidirectional Charge Exchange Spectroscopy in CHS
- 2.3 Alignments and Calibrations of Equipments

Chapter 3. Preparatory Measurements and Considerations

- 3.1 Apparent Wavelength Shift
 - 3.1.1 Interference lines
 - 3.1.2 Spectral Fine Structure of H-like Ions
- 3.2 Back Ground Radiation
 - 3.2.1 Effect of Cold Neutrals
 - 3.2.2 Pluming Effect
- 3.3 Neutral Beam Density
 - 3.3.1 Measurements of the Initial Density Profile
 - 3.3.2 Beam Attenuation

Chapter 4. Poloidal Flow Measurement Results and Discussions

- 4.1 Measured Velocity and Density Profiles
- 4.2 Comparison with the Momentum Balance Equation
- 4.3 Poloidal Flow Conservation
- 4.4 Parallel Force Balance in the Outward Shifted Configuration (Future Theme)
- 4.5 Effect of Neutral and Impurity Flux from the Inner Wall

Chapter 5. Conclusion

References

Appendix1. Measurements of the Asymmetry of Toroidal Rotation.

Chapter 1

Introduction

1.1 Overview

The radial electric fields in magnetically confined toroidal plasmas have been recognized to play an important role in plasma confinements. For example, they change the neoclassical ripple loss in the low collisionality regime[1] and the fast ion orbits[2] in helical devices. They are also the important parameter to trigger the L/H transition and to characterize L/H-modes in tokamak plasmas[3]. Therefore many efforts to study the radial electric fields experimentally have been performed. One of the most powerful methods is the measurements of the rotations velocities of impurity ions by Doppler shift. Radial electric field and rotation velocity are determined by the gradient of electrostatic potential and ion pressure, which are considered to be surface quantities, and thus have variation along the magnetic surfaces depending on the surface configuration. Especially, difference of the rotation velocity between the inside and the outside of torus and poloidal flow conservation in both sides are important to study the toroidal effects on the determination of the plasma rotation[3]. In the plasmas with $M_p \ll 1$ where M_p is the poloidal Mach number, this plasma flow is incompressible. The compensation of inside/outside asymmetry of perpendicular flows by the parallel flows for the incompressible flow conservation is the one of the most basic concept in neoclassical theory[4]. The compressible flows were discussed in the plasmas with $M_p \sim 1$ [5-6], and these theoretical studies are extended in recent H-mode theory[7-8]. However, the difference of the velocities and/or flux between the inside and the outside have never been examined.

In the poloidal rotation measurements in many tokamaks[9-12], only

the poloidal rotation velocities in the outsides were reported because it is difficult to install the observation chords viewing vertically the insides of torus into the narrow space between coils. Another severe difficulty in measuring the plasma velocities is the calibration of mechanical wavelength offset of spectrometers of $\sim 0.5 \text{ \AA}$. When the spectral line of the reference lamp is measured simultaneously without rotating the grating, the wavelength offset can be calibrated. This kind of calibration had been tried using Tl line ($\lambda = 5350.46 \text{ \AA}$) in the toroidal rotation measurement using CVI line ($\Delta n = 8-7$, $\lambda = 5290 \text{ \AA}$) in W7-AS[13]. In this experiment, the measured wavelength range was wide enough to cover both of the Tl line and the CVI line. However, the wide covering range ($> 60 \text{ \AA}$) is incompatible with high wavelength resolution ($\sim 0.1 \text{ \AA/pixel}$). To measure the absolute value of rotation velocity canceling this offset without the reference line, it needs the observation along the opposite viewing directions like the measurements in ASDEX[11]. Therefore, in past plasma rotation measurements using the observation from one direction only, some assumptions or approximations about the plasma rotation velocity profiles are used. In the past measurements of poloidal rotation velocity in Heliotron/Torsatron devices[14-15] the averages of the measurement results in both sides was used as the rotation 'velocity' and/or the radial 'electric field' to 'cancel' the offset. Another method for these poloidal rotation measurements was assuming the wavelength shift observed at the center chord to be zero. However, the accuracy of the measured velocities is dominated only by that at the center chord in this method. Therefore the velocity difference in the inside and the outside of the torus have never been discussed with this method. In toroidal rotation measurements in NBI heated plasmas[16-18], the wavelength shifts in OH phase were often assumed to be zero.

In this thesis, the first observation of the asymmetry of poloidal rotation velocity and density of fully ionized impurity ions on the inside and outside of the torus in the Compact Helical System(CHS) is presented.

CHS is a Heliotron/Torsatron type helical torus with the poloidal period number $l=2$. The past toroidal rotation measurement in CHS clarified the strong toroidal viscosity due to the helical ripple in the outward shifted configuration.[18-19]. This damping of toroidal flow is strong in peripheral region where the helical ripple is large. However, the poloidal rotation of impurity ions mainly driven by radial electric field determined by the ambipolar condition of electron and ion loss [20-22] is also large in this peripheral region[15,23]. Therefore the compensation of the asymmetry of inside and outside perpendicular flows by the parallel flows becomes difficult in this region. When the electrostatic potential is the surface quantity and the poloidal rotation of ions is mainly $E \times B$ drift, the flow, especially of the impurity ions having low pressure, should be compressible in spite of small poloidal Mach number. Otherwise the electrostatic potential is not the surface quantity or the poloidal rotation of impurity ions is not $E \times B$ drift. Investigating this problem is easier in low aspect ratio devices, therefore this poloidal rotation measurement in CHS, with the lowest aspect ratio $R_0/a=5$ in helical devices, is an important and interesting theme.

For this purpose, we constructed a charge exchange spectroscopic system with bidirectional viewing optics to measure the absolute value of poloidal rotation velocity on inside and outside of the torus at a vertically elongated section.

1.2 Compact Helical System

CHS is a Heliotron/Torsatron type helical torus(poloidal period number $l=2$, and toroidal period number $m=8$) with the major radius $R_0=1\text{m}$ and the averaged minor radius $a=0.2\text{m}$ (Figure 1.1 and Table 1.1). The rotational transform ($\iota/2\pi = R_0 B_\theta / a B_\phi$) and the helical ripple (ϵ_h) at the plasma edge are ~ 1 and ~ 0.3 , respectively. The magnetic

field strength is 0.9-1.8T. Figure 1.1 shows the schematic view of the CHS device with heating and diagnostic systems. Two heating neutral beams (one is co-injection and the other is counter-injection) can be injected tangentially. The accelerating voltage and the power of each beams are <40kV and <1MW, respectively. The electron temperature and density profiles are measured with a 24ch YAG Thomson scattering with the time resolution of 4ms and a HCN laser interferometer.

As reported previously[15,23], the typical plasma parameter of NBI heated plasmas corresponds to the plateau regime defined in the neoclassical theory and the negative radial electric fields of several tens of V/cm was observed. This negative electric fields in NBI heated plasmas was observed also by the recent heavy ion beam probe(HIBP) measurements[24]. Therefore the poloidal rotation measurements should have the resolution to detect the velocities of a few km/s. These values are smaller than that of the edge poloidal rotation in the H-mode plasmas of tokamaks[10-13,25]. To establish the measurement technique to detect the difference of the velocities on inside and outside of the torus is the first step of this study.

The magnetic surface configuration and the toroidal viscosity due to the helical ripple change depending on the major radius of the vacuum magnetic axis position(R_{ax}). The magnetic surface configuration, the rotational transform and the helical ripple in the typical inward shifted configuration($R_{ax}=92.1\text{cm}$) and the typical outward shifted configuration($R_{ax}=99.5\text{cm}$) are shown in Figure 1.2 and Figure 1.3. Figure 1.4 shows the dependence of the parallel viscosity on the magnetic axis position[19]. The measurements of the asymmetry of the poloidal flow were carried out for some magnetic surface configurations to investigate the dependence on these parameters.

1.3 Outline of Thesis

This thesis is composed of five chapters. In chapter 2, the diagnostics principles of charge exchange spectroscopy and the hardware for the poloidal flow measurements in CHS are presented.

For the purpose mentioned above, there are some technical subjects in this diagnostics such as correcting apparent Doppler shifts not due to the plasma rotation, and the subtracting background radiation to obtain the correct rotation velocity and the density of fully ionized impurity. These subjects are discussed in chapter 3.

The experimental results and the discussions about the inside/outside asymmetry of the poloidal rotation velocity and the density of fully ionized carbon ions are described in chapter 4. To investigate the mechanism determining the inside/outside asymmetry of the velocity and the density, the electrostatic potential calculated using the momentum balance equation and the poloidal flux conservation are discussed here. The effects of the neutral and impurity fluxes from the inner wall on the measured density profile are also discussed.

Finally, these results are concluded in chapter 5.

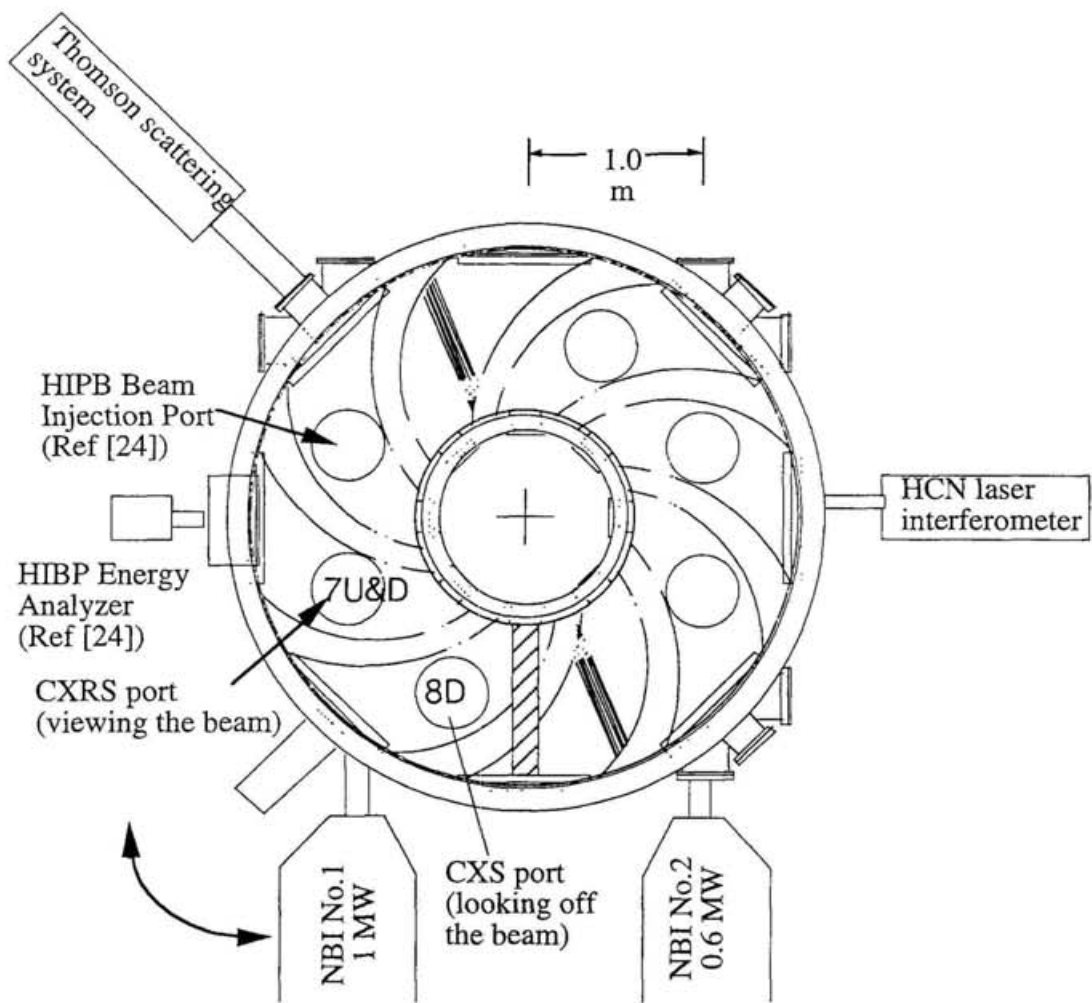


Figure 1.1 (a): A schematic view of the Compact Helical System (top view).

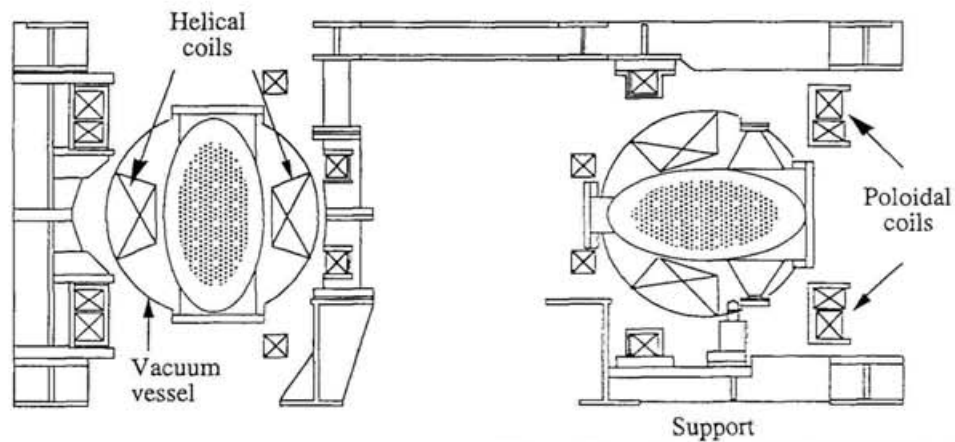


Figure 1.1 (b): A schematic view of the Compact Helical System (side view).

Parameter	Value
Major radius	1.0 m
Averaged minor radius	0.2 m
Aspect ratio	5
Poloidal period number	2
Toroidal period number	8
Pitch parameter	1.25
Pitch modulation	0.3
Field strength	~2T
Rotational transform (center in vacuum)	0.3
(edge in vacuum)	0.8~1.0
Neutral beam power	1.1MW at 40kV 0.7MW at 36kV
NBI pulse length	1 sec
ECH pulse length	100 ms
ECH power	500kW at 53GHz
ICRF power	1.5MW
ICRF frequency	6~28MHz

Table 1.1: Specification of CHS

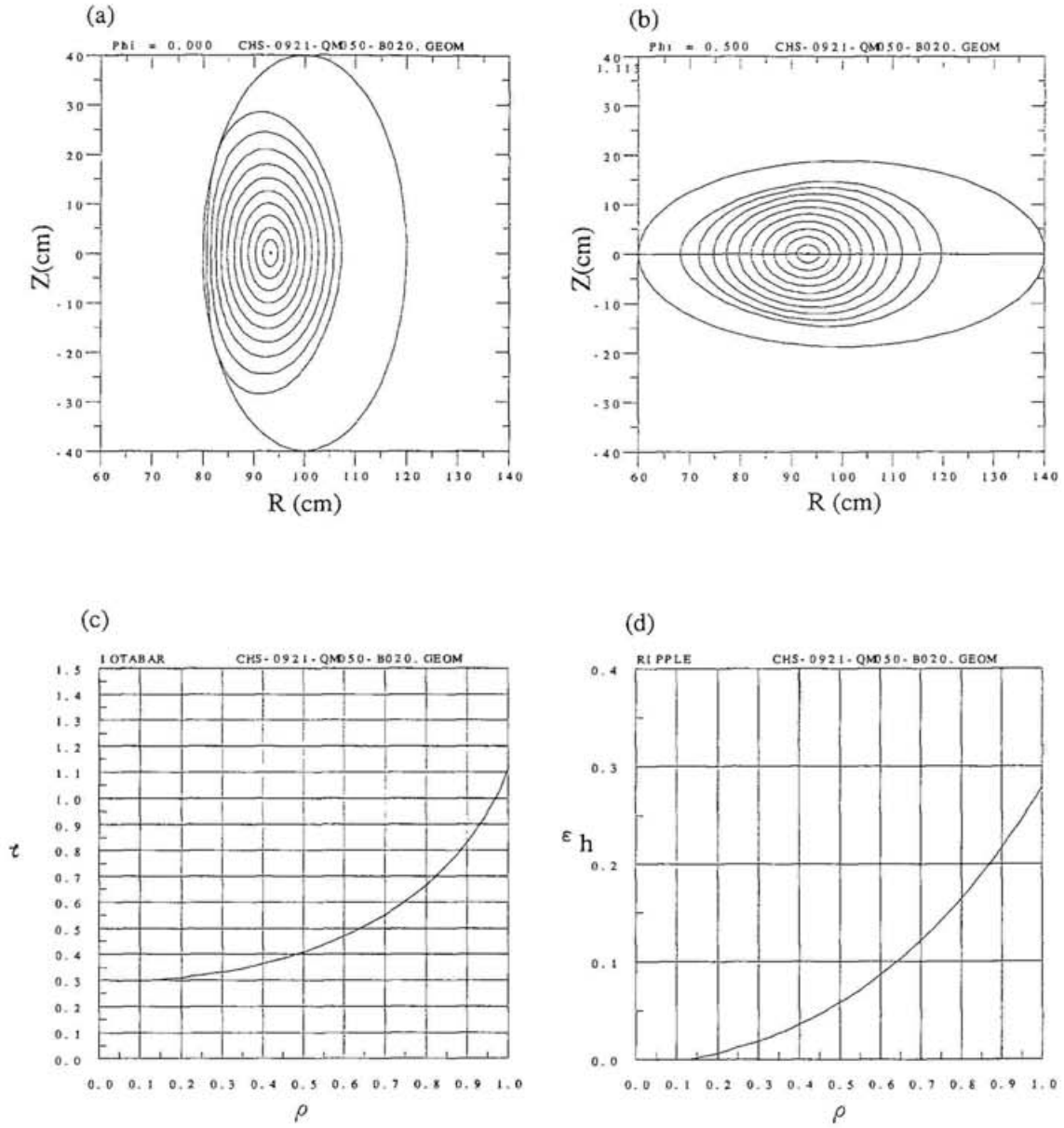


Figure 1.2 Magnetic Field in the Inward Shifted Configuration ($R_{ax}=92.1\text{cm}$ $\beta=0.2\%$)

- (a) Magnetic Surface at a Vertically Elongated Section
- (b) Magnetic Surface at a Horizontally Elongated Section
- (c) Rotational Transform τ
- (d) Helical Ripple ϵ_h

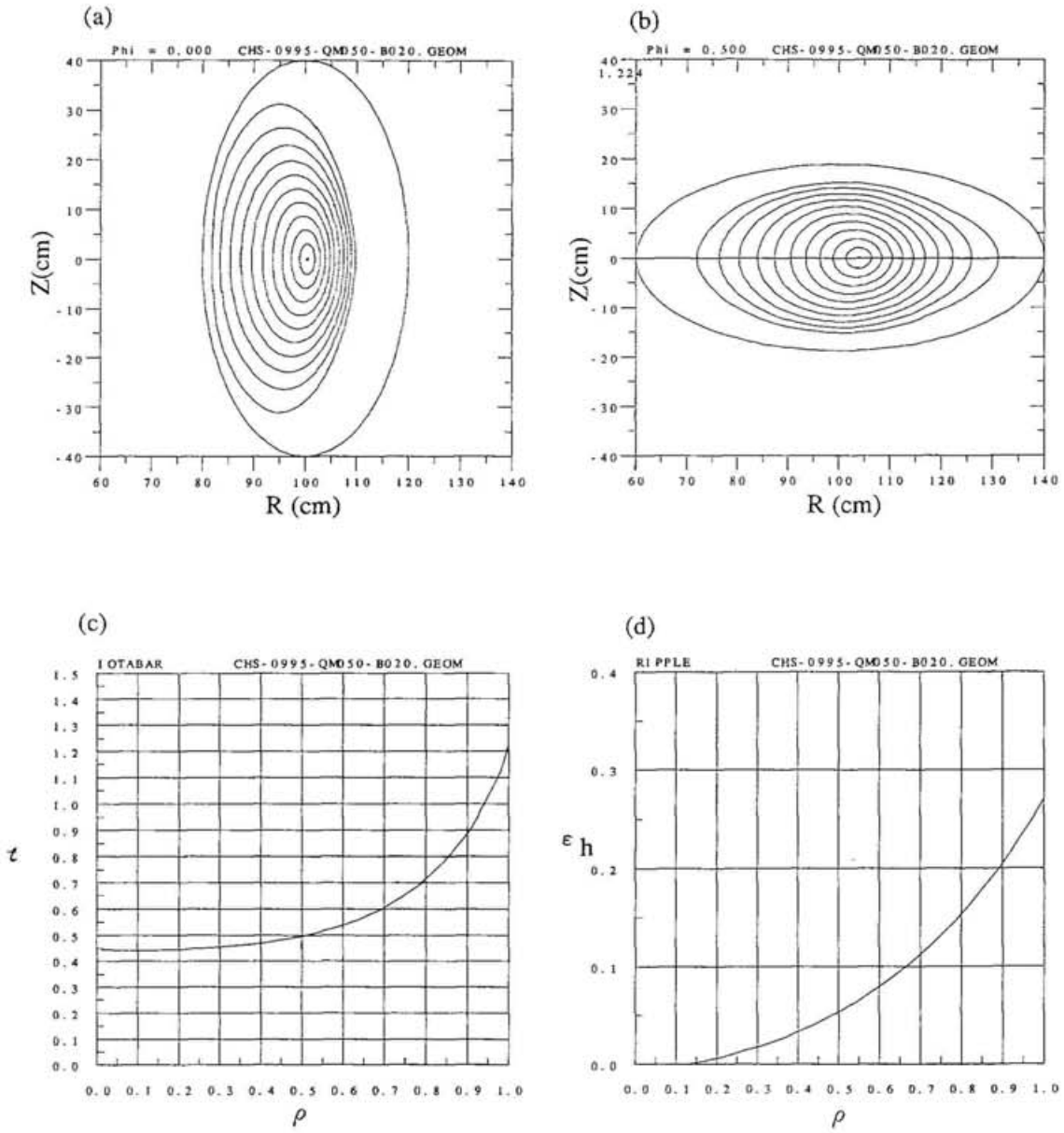


Figure 1.3 Magnetic Field in the Outward Shifted Configuration ($R_{ax}=99.5\text{cm}$ $\beta=0.2\%$)

- (a) Magnetic Surface at a Vertically Elongated Section
- (b) Magnetic Surface at a Horizontally Elongated Section
- (c) Rotational Transform τ
- (d) Helical Ripple ϵ_h

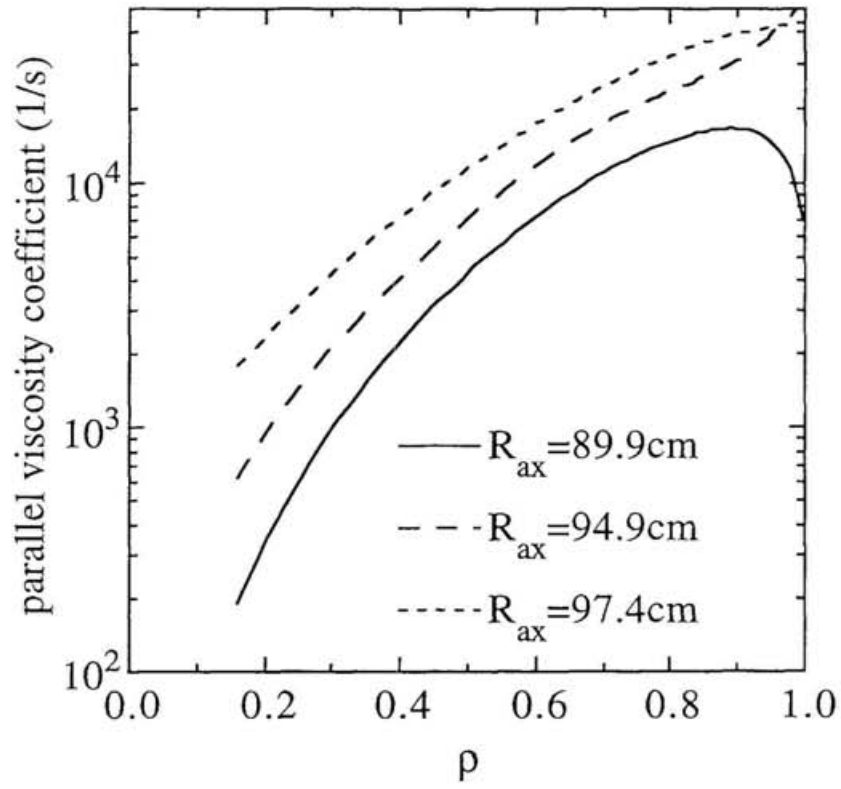


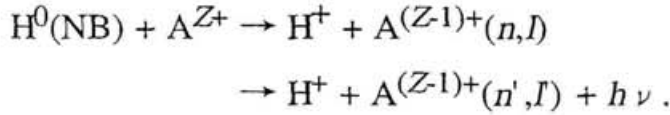
Figure 1.4 Dependence of the parallel viscosity coefficient on the magnetic axis position (R_{ax}) (Ref[19])

Chapter 2

Charge Exchange Spectroscopy System in CHS

2.1 Diagnostics Principles

The charge exchange spectroscopy(CXS) is the widely used active diagnostic method to measure the spatial distributions of the plasma rotation and ion temperature. Since the charge exchange recombination emission was recognized in the ORMAK tokamak[26], extensive studies have been performed and the usefulness of CXS has been established. This measurement technique uses the charge exchange recombination reaction of fully ionized ions with a neutral beam expressed as



where $\text{H}^0(\text{NB})$ and A^{Z+} express the beam hydrogen atom and the fully ionized impurity ion with charge Z , respectively. n,l and n',l are the principal and the angular momentum quantum number of the recombining excited state and the state into which the radiative transition occurs, respectively. These reactions often accompany the emission of spectral lines in the visible wavelength region which has the advantages of low attenuation through the optical fiber, and of a large Doppler shifts and broadenings. The life times of excited states are usually shorter than the ion cyclotron period, therefore this shift and broadening express the velocity distribution of A^{Z+} ions. The CXS measurements of the bulk ions(H/D) are difficult since the $\text{H}_\alpha/\text{D}_\alpha$ or $\text{H}_\beta/\text{D}_\beta$ lines are usually obscured by intense thermal emission from the plasma edge and by the emission from the beams themselves. Therefore the transitions from the highly excited states in light impurity ions are used. Carbon impurity has

been used in many devices, since carbon is one of the main impurities sputtered from limiters or diverter plates and fully ionized in most plasmas. The $\Delta n=7-6$ ($\lambda=3434 \text{ \AA}$) and $\Delta n=8-7$ ($\lambda=5290 \text{ \AA}$) transitions in C^{5+} ion are used. The $\Delta n=8-7$ ($\lambda=5290 \text{ \AA}$) transition is more desirable because of the advantage of the absence of interfering impurity lines nearby. The apparent wavelength shift caused by the interfering impurity line at $\lambda=3434 \text{ \AA}$ observed in CHS is shown in Chapter 3 of this thesis.

Principally, the emission originates from the volume defined by the intersection of the neutral beams and the line of sight. However, radiation from the plasma periphery due to the charge exchange of A^{Z+} ions with thermal hydrogen atoms and/or the electron impact excitation of incompletely ionized $A^{(Z-1)+}$ ions is superimposed. In order to obtain the temperature, velocity and density of A^{Z+} ions in the intersection correctly subtracting this radiation from the periphery ("cold component", "background"), following techniques have been used.

- 1) The beam modulation technique[27]
- 2) Double Gaussian fitting[28,29]
- 3) Reference channels looking off the neutral beam line[17]

In the poloidal flow measurement in CHS, we adopted the reference channel method to obtain the velocity and density of A^{Z+} ions only even in the periphery since the double Gaussian fitting is not effective in the periphery where the Doppler broadening of the charge exchange radiation due to the beam becomes small comparably to that of background radiation. These need and the validity of the use of reference channel is discussed in Section 3.2

2.2 Bidirectional Charge Exchange Spectroscopy in CHS

Figure 2.1 shows the schematic arrangement of the CXS in CHS. One of the heating neutral beam lines (NBI#1) is used for CXS. In order to cancel the wavelength offset of the spectrometer, this measurement system uses two fiber arrays (30ch/array) to view vertically the beam line from up and down sides simultaneously at one vertically elongated section (port #7). The average of the wavelength measured from both sides gives the wavelength without Doppler shift ($\Delta \lambda = 0$). And the background radiation is measured at another vertically elongated section (port #8) where the beams don't pass. The observation chords are situated in the range of $0.845\text{m} \leq R \leq 1.106\text{m}$, where R is the major radial position, at each ports. All of these fibers (90ch) are connected to a M-100 spectrometer's slit and the diffraction image is detected with a CCD detector with a image intensifier(Hamamatsu C4336-06MR2). The time resolution of this detector is 20ms. The specifications of this system are listed in Table 2.1.

2.3 Alignments and Calibrations of Equipments

Alignments and Calibrations peculiar to the multi-chord spectroscopic measurements using two dimensional CCD detectors are described in Ref [17]. Also in the system for CHS,

- 1) wavelength dispersion
- 2) instrumental width
- 3) the nonlinearity of relative sensitivity
- 4) the absolute sensitivity

are calibrated. These results are also listed in Table 2.1. The wavelength dispersion and the instrumental width are calibrated using the Hg lines. Figure 2.2 shows the sensitivity nonlinearity of CCD measured using ND filters. These measured values are fitted by the polynomial

$$I_r = -0.00046 + 1.00 \times X - 1.3031 \times X^2 + 5.5175 \times X^3 - 8.5755 \times X^4 + 4.5505 \times X^5 \quad (1),$$

where I_r is the relative input signal level and X is the CCD output signal level normalized by the saturation level. The distortion of the measured spectral profiles are corrected using this polynomial.

Figure 2.3(a) shows the schematic arrangement for the calibration of the absolute sensitivity of this system. The image of the filament of the tungsten ribbon type standard lamp is made on the lens of the collimator. The radiant density[photon/cm²/Å/steradian/s] of this image is identical with that of the filament, therefore the photon input rate per unit wavelength[photon/Å/s] to the fiber core are can be expressed as,

$$\text{photon input rate[photon/Å/s]} = \beta_L \pi r_b^2 \pi (r_c/l_c)^2 \quad (2),$$

where β_L , r_b , r_c , l_c are the radiant density of the lump, the beam radius of the collimator, the radius of the fiber core, and the distance between the fiber aperture and the lens of the collimator, respectively.

With these parameters, the photon input rate into the fiber core in the the plasma measurements shown in Figure 2.3(b) also can be written as

$$\begin{aligned} \text{photon input rate[photon/Å/s]} &= \beta_P \pi (r_c l_f/l_c)^2 \pi (r_b/l_f)^2 \\ &= \beta_P \pi r_b^2 \pi (r_c/l_c)^2 \end{aligned} \quad (3),$$

where β_P and l_f are the radiant density of the surface of the emitting region of the plasma and the distance between the lens of the collimator and the image of the fiber aperture (at the surface of the emitting region). It has the same form as Eq.(2), therefore the measured signal level in the arrangement shown in Figure 2.3(a) gives the overall sensitivity of the spectrometer system including the fiber and the collimator.

Figure 2.4 shows the ratio of the measured output signal level of the system I_r to the radiant density of the lump, where I_r is the signal level after the correction of the sensitivity non-linearity expressed by Eq.(1).

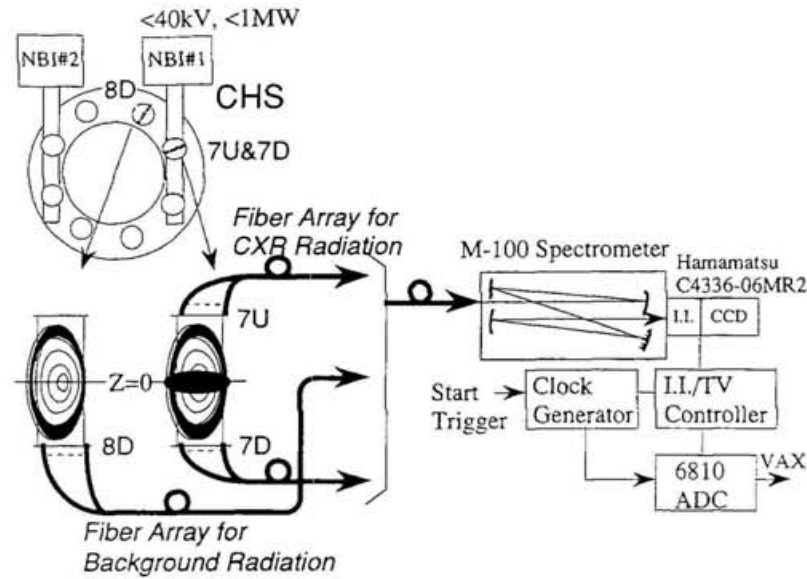


Figure 2.1 Schematic Arrangement of the Bidirectional Charge Exchange Spectroscopy (CXSE) in CHS

Fiber Arrays

viewing chords 7mm ϕ parallel beam \times 30ch/array
 fibers 125 μ m diam step-index quartz with 100 μ m core (attenuation :16dB/km in visible range)

Spectrometer (Jasco M100-T)

focus length 1000mm
 f 8.7
 grating 2400l/mm
 dispersion curve $\Delta \lambda$ ($\text{\AA}/\text{pixel}$) = $-0.1218 - 3.60 \times 10^{-6} \times \lambda + 1.545 \times 10^{-9} \times \lambda^2$
 where λ is the wavelength [\AA] (0.1 $\text{\AA}/\text{pixel}$ at $\lambda = 5000 \text{\AA}$)
 instrumental width 3.6pixel

CCD detector with a image intensifier (Hamamatsu C4336-06MR2)

effective image size 11.6mm \times 8.7mm
 I.I - CCD coupling fiber coupling
 vertical scanning frequency 50kHz (CCIR)
 nonlinearity correction curve
 relative input (I_r) = $-0.00046 + 1.00 \times X - 1.3031 \times X^2 + 5.5175 \times X^3 - 8.5755 \times X^4 + 4.5505 \times X^5$
 where X is the CCD output normalized by the saturation level (Figure 2.2)

Overall Sensitivity

radiant density = 6.3×10^{13} photon/cm²/ \AA /sr/s at the half of the saturation level in the condition of $\lambda = 6500 \text{\AA}$, gain=6.0 (The detail dependence on the condition are shown in Figure 2.4)

ADC (Lecroy 6810) & Clock Generator

sampling pixel 256 \times 243 (H \times V)
 accuracy 12bit
 sampling clock 5MHz
 frame/shot 8

Table 2.1 Specifications of the equipments in the CXSE system

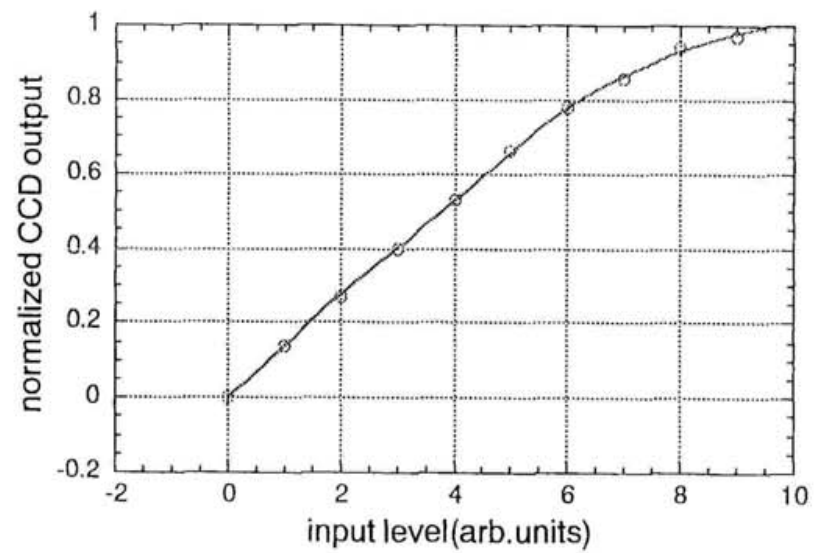


Figure 2.2 Correction curve for the sensitivity nonlinearity of CCD.

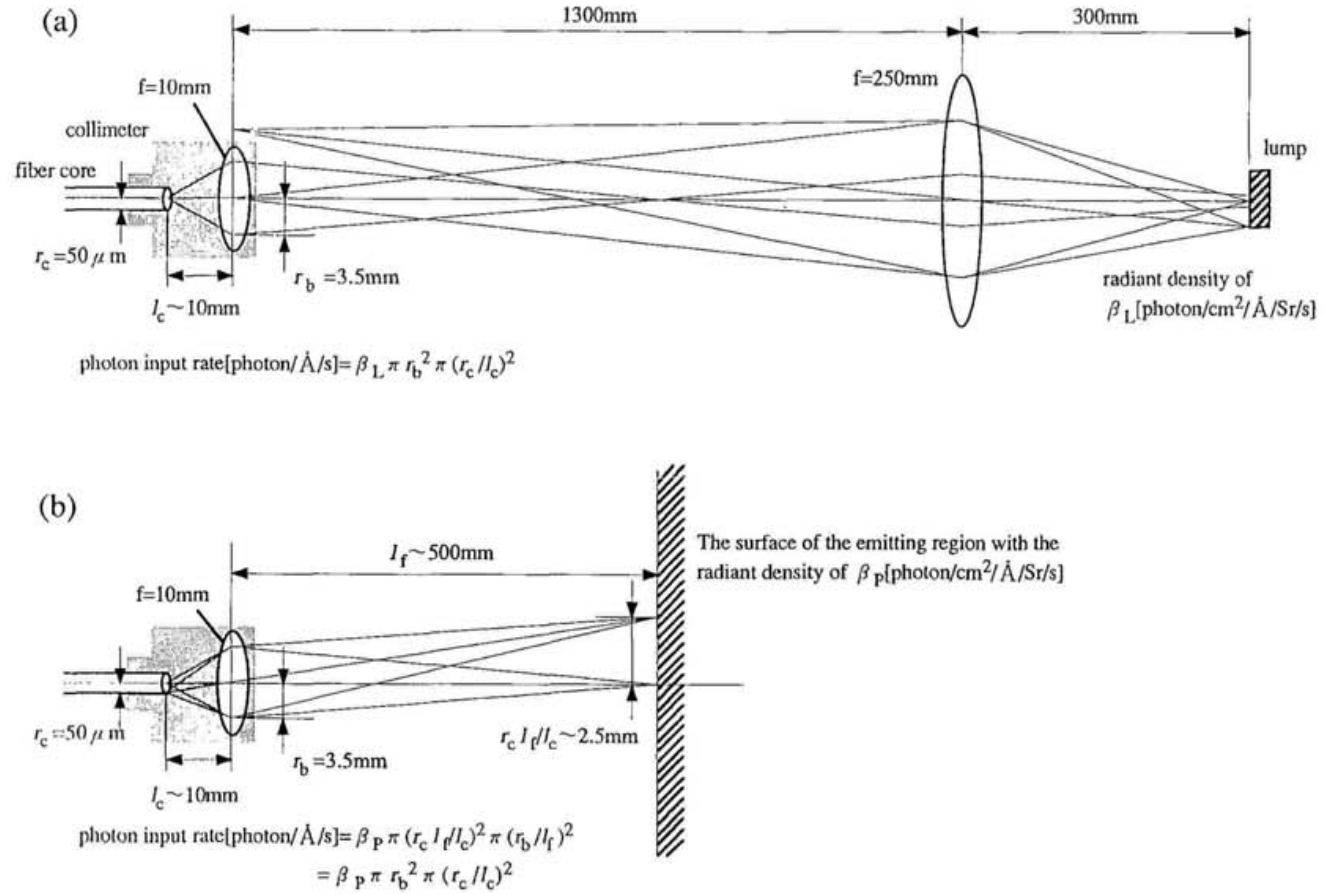


Figure 2.3 The comparison of the schematic arrangements for the absolute sensitivity calibration and that for the plasma measurements.

(a) The absolute sensitivity calibration.

In this arrangement, the photon input rate[photon/ $\text{\AA}/\text{s}]$ into the fiber core is expressed as $\beta_L \pi r_b^2 \pi (r_c / l_c)^2$ since the image of lump has the identical radiant density as that of the lump, where β_L , r_b , r_c , l_c are the radiant density of the lump, the beam radius of the collimator, the radius of the fiber core, and the distance between the fiber aperture and the lens of the collimator, respectively.

(b) The plasma measurements.

In this arrangement, the photon input rate into the fiber core is expressed as $\beta_P \pi (r_c l_f / l_c)^2 \pi (r_b / l_f)^2 = \beta_P \pi r_b^2 \pi (r_c / l_c)^2$, where β_P and l_f are the radiant density of the surface of the emitting region of the plasma and the distance between the lens of the collimator and the image of the fiber aperture (at the surface of the emitting region).

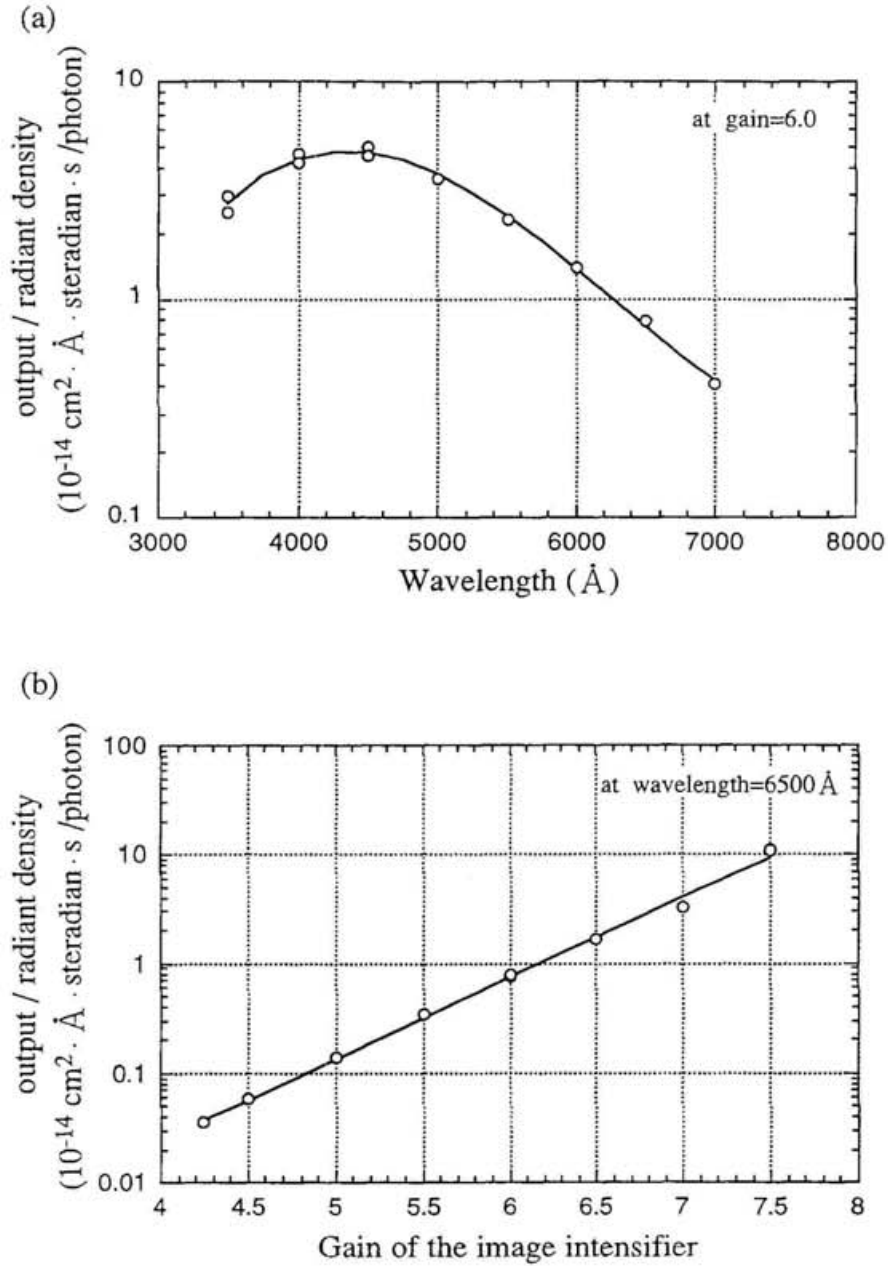


Figure 2.4 The dependence of the absolute sensitivity on the wavelength(a) and the gain (accelerating voltage) of image intensifier(b). These figures show the ratio of the output signal of the system I_T to the radiant density [$\text{photon}/\text{cm}^2/\text{\AA}/\text{sr}/\text{s}$] of the lump, where I_T is calculated with Eq.(1).

The spatial resolution and/or the accuracy in the major radius direction(ΔR) is $\pm 5\text{mm}$. It's dominated by (1) the beam diameters of the chords($7\text{mm } \phi$), (2) the sampling step size(pixel) of CCD image($45\mu\text{m}$ in vertical direction. 2.8pixel/fiber) and (3) the cross talk between channels($\sim 30\%$) on the CCD image.

The preliminary plasma rotation measurement result with this system showed the large discrepancy between the spatial distribution profile of Doppler shifts measured from the upper viewing array and that from lower viewing array as shown in Figure 2.5. This discrepancy was mainly caused by the intrinsic wavelength shift of the spectrometer itself depending on the position in the slit direction. Figure 2.6 shows this dependence calibrated with Hg lines($\lambda = 366\text{nm}$ and 546nm). This shift is corrected in the derivation of the spectral profiles of each fiber channels from the CCD image.

The local structure of this dependence comes from the displacement of the fibers in horizontal direction since this system uses fibers themselves as the entrance slit by opening the slit width wider than the diameter of fibers. The global structure of this dependence comes from the distortion of diffraction image which depends on wavelength. It can be shown as follows. This distortion is expressed as

$$\delta x = m \lambda / (d R_f \cos \beta) z^2$$

where m and λ are the order and the wavelength of interest; $d=0.417\mu\text{m}$, $R_f=1\text{m}$, $\beta \sim 0^\circ$ and z are the groove spacing of the grating, the focal length, the exit angle of the spectrograph, and the distance from the center of the slit, respectively. Figure 2.7 shows the difference in the diffraction image of the fibers on the CCD for $\lambda = 5460\text{\AA}$ and $\lambda = 3655\text{\AA}$ in Figure 2.3, i.e. $(\Delta \lambda|_{\lambda=5460\text{\AA}} - \Delta \lambda|_{\lambda=3655\text{\AA}})P$, where $P=36\mu\text{m}$ is the pixel size in horizontal direction. This difference shows an agreement with the calculated value of $(\delta x|_{\lambda=5460\text{\AA}} - \delta x|_{\lambda=3655\text{\AA}})$.

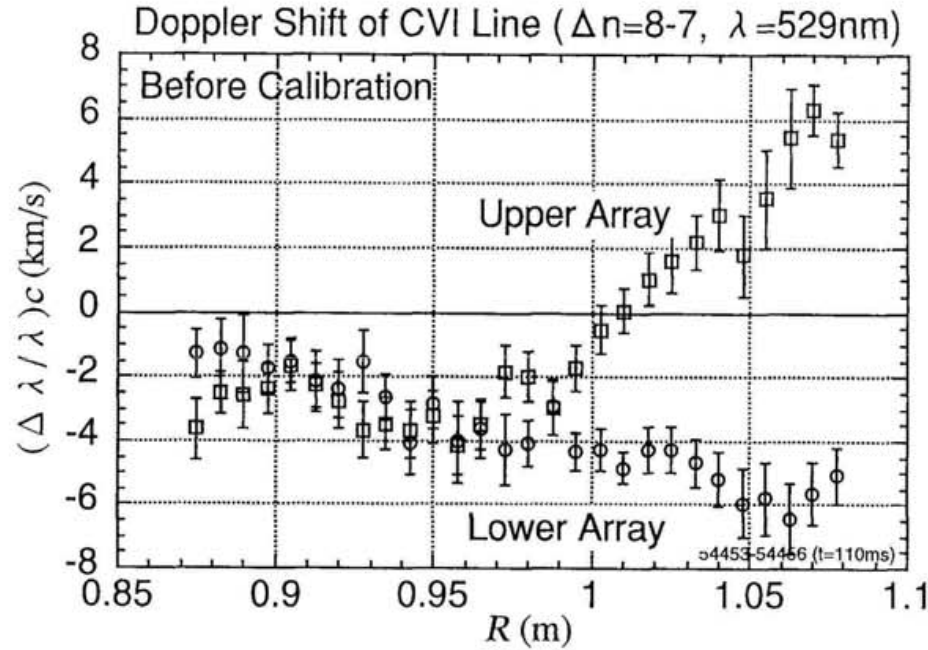


Figure 2.5 The intrinsic wave length shift of the spectrometer itself found in plasma measurements. The Doppler shifts measured via the upper viewing array ('7U') and the lower viewing array ('7D') without subtracting the background radiation should have the same magnitude of reversed Doppler shifts (i.e. one is the blue shift and the other is the red shift) at each observation chords. This result, however, does not show this upper/lower symmetry.

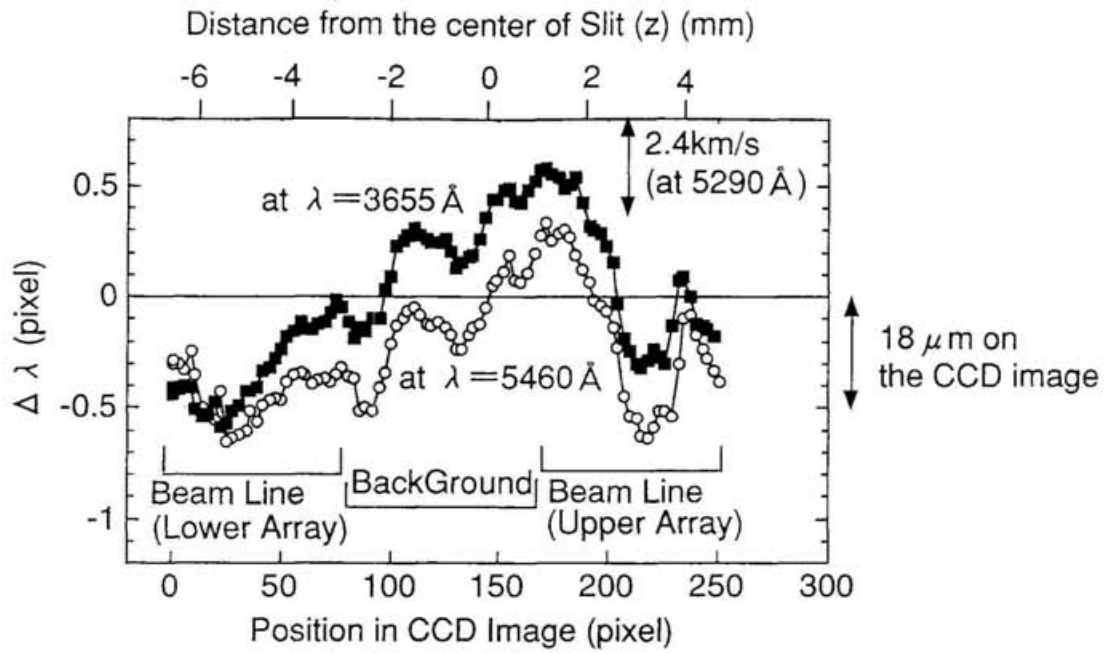


Figure 2.6 The dependence of wavelength shifts $\Delta \lambda$ on the position in the vertical direction of the diffraction pattern (CCD image). Marks ○ and ■ indicate fiber channels.

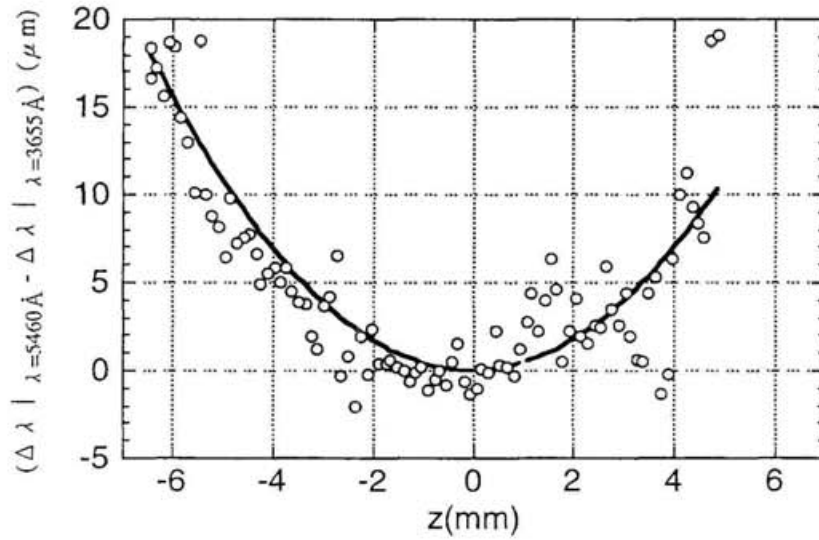


Figure 2.7 The difference in the diffraction patterns on the CCD image for $\lambda = 5460 \text{ \AA}$ and $\lambda = 3655 \text{ \AA}$ in Figure 2.4. The solid curve is the calculated value of $m(5460 \text{ \AA} - 3655 \text{ \AA}) / (d R_f \cos \beta) z^2$, where Z is the distance from the center of the slit. The global structure of the diffraction patterns and their dependence on wavelength shown in Figure 2.4 can be explained by the distortion expressed as $\delta x = m \lambda / (d R_f \cos \beta) z^2$.

Chapter 3

Preparatory Measurements and Considerations

3.1 Apparent Wavelength Shifts

3.1.1 Interference lines

The Doppler shifts measured via the upper ('7U') and lower ('7D') viewing arrays without subtracting the background radiation should have the same magnitude of the reversed Doppler shifts (i.e. one is the blue shift and the other is the red shift) at each observation chords. When the discrepancy between the magnitudes of results in both arrays exists, it means the apparent Doppler shift not due to the plasma rotation. The bidirectional viewing can detect this kind of apparent shifts not due to the plasma rotation. For example, the preliminary measurement results of CVI lines in visible region ($\Delta n=8-7$, $\lambda=5290 \text{ \AA}$ and $\Delta n=7-6$, $\lambda=3434 \text{ \AA}$.) with this system is shown in this section.

At first, the apparent shift caused by the interference line at $\lambda=3434 \text{ \AA}$ is shown in Figure 3.1.1. There are relative blue shifts at the peripheral low temperature region. This direction is opposite to the apparent shift due to the spectral fine structure described below. When this apparent shift is appears in the peripheral region, the blue shift of the background radiation at $\lambda=3434 \text{ \AA}$ sometimes reaches $(\Delta \lambda / \lambda)c \sim -10 \text{ km/s}$ and is quite large (by factor 2) compared with that at $\lambda=5290 \text{ \AA}$. These results suggest that there are spectral lines of other impurity ions (for example, OVI) on the near blue side of CVI $\lambda=3434 \text{ \AA}$ line, in the background radiation.

This apparent Doppler shift cannot be corrected since the intensity ratio of this interference line to the CVI line is unknown, therefore only the line at $\lambda=5290 \text{ \AA}$ was used for the poloidal rotation measurements after this fact was recognized.

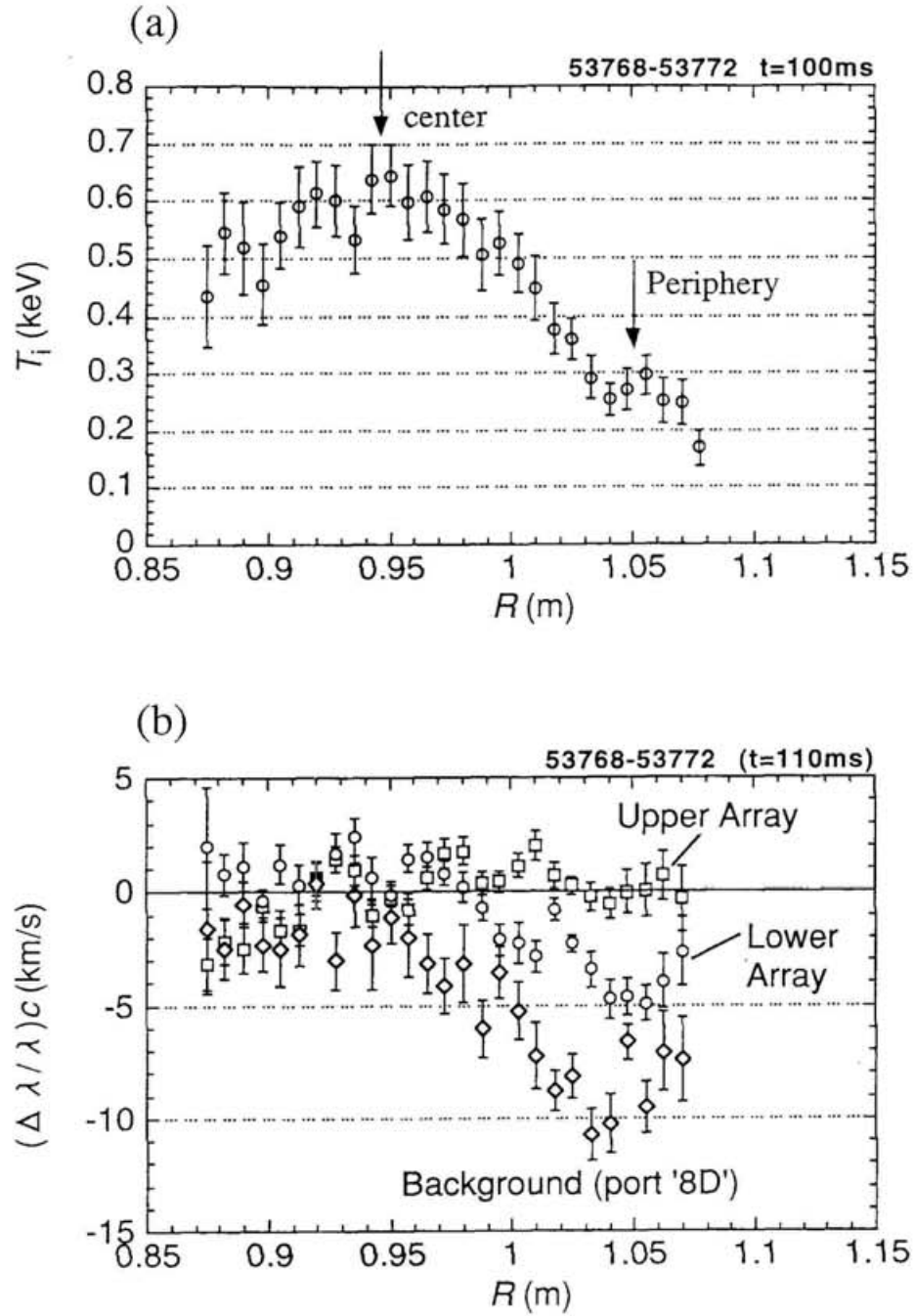


Figure 3.1.1. The apparent blue shifts at peripheral low temperature region due to the interference line at $\lambda = 3434\text{\AA}$.

In the discharge with the condition of $R_{ax}=92.1\text{cm}$,

$$B_t=1.7\text{T(}CCW), \bar{n}_e=1.5 \times 10^{13}\text{cm}^{-3}, W_p=1.5\text{kJ.}$$

(a) The ion temperature profile to show the position of the center and the periphery.

(b) The wave length shift(before subtracting background)

3.3.2 Spectral Fine Structure of H-like Ions

Figure 3.1.2 shows the spatial distribution of the wavelength shifts of the CVI line($\Delta n=8-7$, $\lambda=5290 \text{ \AA}$) given by the least square fitting of single Gaussian profile. The apparent Doppler shift to red-side of the CVI line is recognized in peripheral low ion temperature($T_i \sim 100\text{eV}$) region. Another example of apparent shifts depending on the ion temperature was observed in the discharge shown in Figure 3.1.3.1. The wavelength shifts of the CVI line($\Delta n=7-6$, $\lambda=3434 \text{ \AA}$) in the NBI heated phase($t=130\text{ms}$) and the after-glow recombining phase($t=170\text{ms}$) with the ion temperature of 30eV are shown in Figure.3.1.3.2. The shifts are given by single Gaussian least square fitting. During NBI heated phase, the wavelength shifts measured from the up and down sides shows the real Doppler shift due to the poloidal rotation. After the NBI pulse was turned off, however, the both arrays show shifts to red-side. Although the apparent blue shift caused by the interference line at the periphery also exists in this discharge, this red shift in low temperature phase is similar to that in the peripheral low ion temperature region observed with the line at $\lambda=5290 \text{ \AA}$.

To explain these apparent Doppler shifts given by single Gaussian least square fitting, the distortion of the spectral profile due to the spectral fine structure of hydrogen-like ions is discussed here. Hydrogen-like ions have the splitting of energy levels due to a relativistic effect expressed in the formula[30].

$$E(n,j) = -\frac{Z^2 R_y}{n^2} \left[1 + \frac{(\alpha Z)^2}{n} \left(\frac{1}{j+1/2} - \frac{3}{4n} \right) \right]$$

where, n is the principal quantum number, j is the total angular momentum, Z is the nuclear charge, R_y is the Rydberg constant and α is the fine structure constant ($=1/137$). The over-estimation of ion

temperature caused by this splitting had been pointed out by Fonck[29]. Although the difference between the 'real' and the 'apparent' ion temperature cannot be directly measured in CXS, a 'real' and an 'apparent' Doppler shift can be distinguished by the observation along the opposite viewing directions.

The intensity ratio of fine structure components depends on the sub-level population. The charge exchange excitation rates[29] were estimated by using the Pengelly and Seaton's theory of collisional transition among degenerate energy levels in the recombining plasmas[31]. From this study, the $n=7$ and 8 states in C^{5+} ion, which can cause the transition with the visible range lines, are considered to be in the 'collisional l-mixed' state in the plasma parameter regime of CHS plasmas. In 'l-mixed' state, the sub-level populations are proportional to statistical weights $(2l+1)/n^2$. Figure.3.1.4 shows the example of observed spectral profile of the CVI line($\Delta n=7-6$, $\lambda=3434 \text{ \AA}$) and the fine structure pattern calculated with this assumption, where the transition probabilities (A-coefficient) are calculated from the oscillator strength listed in Ref[32]. The observed spectral profile has a red-side/blue-side asymmetry, and thus the fitting with the super-position of fine structural component with Doppler broadening shows better agreement with the measured spectrum than the fitting with a single Gaussian profile. Figure.3.1.5 shows the center wavelength of the half-maximum of these calculated spectra. They shifts to the red side with decreasing ion temperature(i.e. Doppler broadening) and total shift in the ion temperature range of hundreds eV corresponds to the velocity error of a few km/s. The measured apparent wavelength without real Doppler shifts $(\Delta \lambda_{\text{upper}} + \Delta \lambda_{\text{lower}})/2 + \lambda_{8-7}$ in the plasma shown in Figure 3.1.2 and the measured apparent wavelength $\Delta \lambda_{\text{recomb}} + \lambda_{7-6}$ in the after-glow recombining phase shown in Figure 3.1.3, where λ_{8-7} and λ_{7-6} are taken to be 5292.082 \AA and 3434.72 \AA respectively for the best fit of the data to the calculated curve, are also

shown for the comparison of the dependence on ion temperature. The dependence of these wavelength on the ion temperature is consistent with the prediction from the fine structure calculation.

This effect causes the velocity error of a few km/s in the peripheral region with the low ion temperature of $<200\text{eV}$. Therefore the spectrum fitting should be done not with a single Gaussian curve but with a distorted profile(multiple Gaussian curve) calculated with statistical weighted sub-level population.

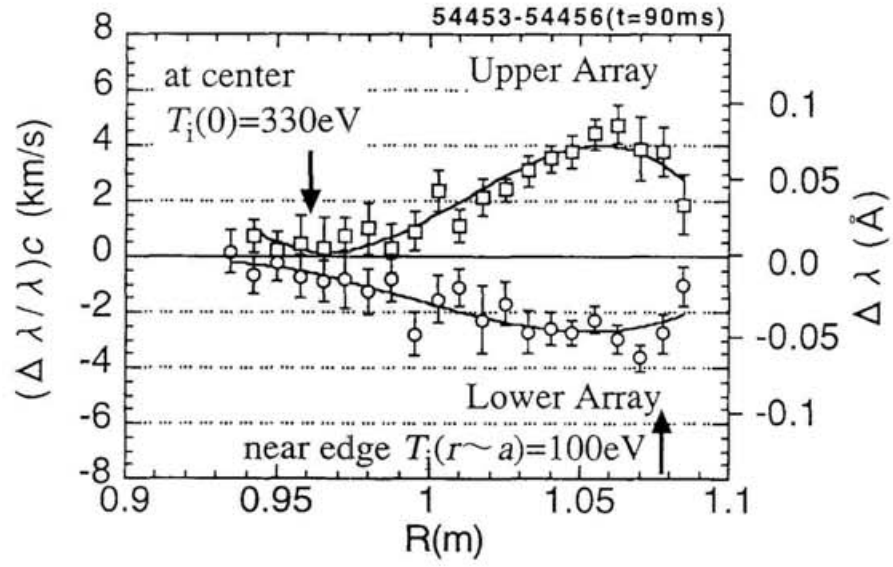


Fig.3.1.2: The wave length shifts measurement result given by single Gaussian fitting at the upper and lower viewing arrays. (CVI; $\Delta n=8-7$, $\lambda=5290\text{Å}$).

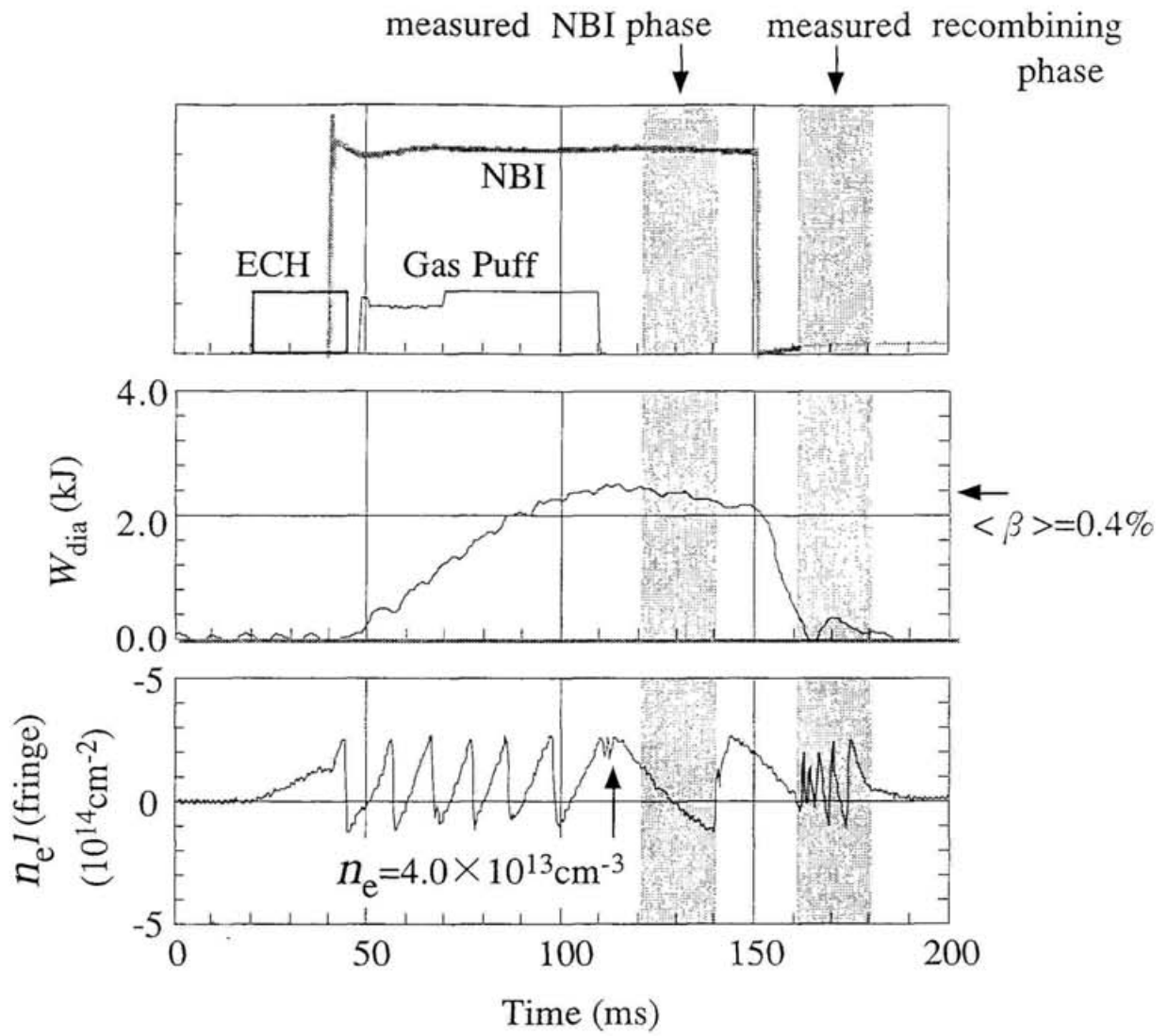


Figure 3.1.3.1 Time behavior of the plasma parameters in the discharge in which the apparent shift in the after-glow recombining phase is examined. The wavelength measurement was done at $t=130\text{ms}$ and $t=170\text{ms}$ with the integration time of 20ms.

This figure shows the typical operation of the NBI heating experiments in CHS.

(a) The heating and gas-puffing scheme.

(b) The stored energy by the diamagnetic measurement. The volume averaged β value $\langle \beta \rangle$ reached to 0.4% in this discharge.

(c) The fringe signal from the center chord of interferometer.

The integrating chord length is $l=52\text{cm}$ and the line averaged electron density n_e reached to $4.0 \times 10^{13} \text{cm}^{-3}$

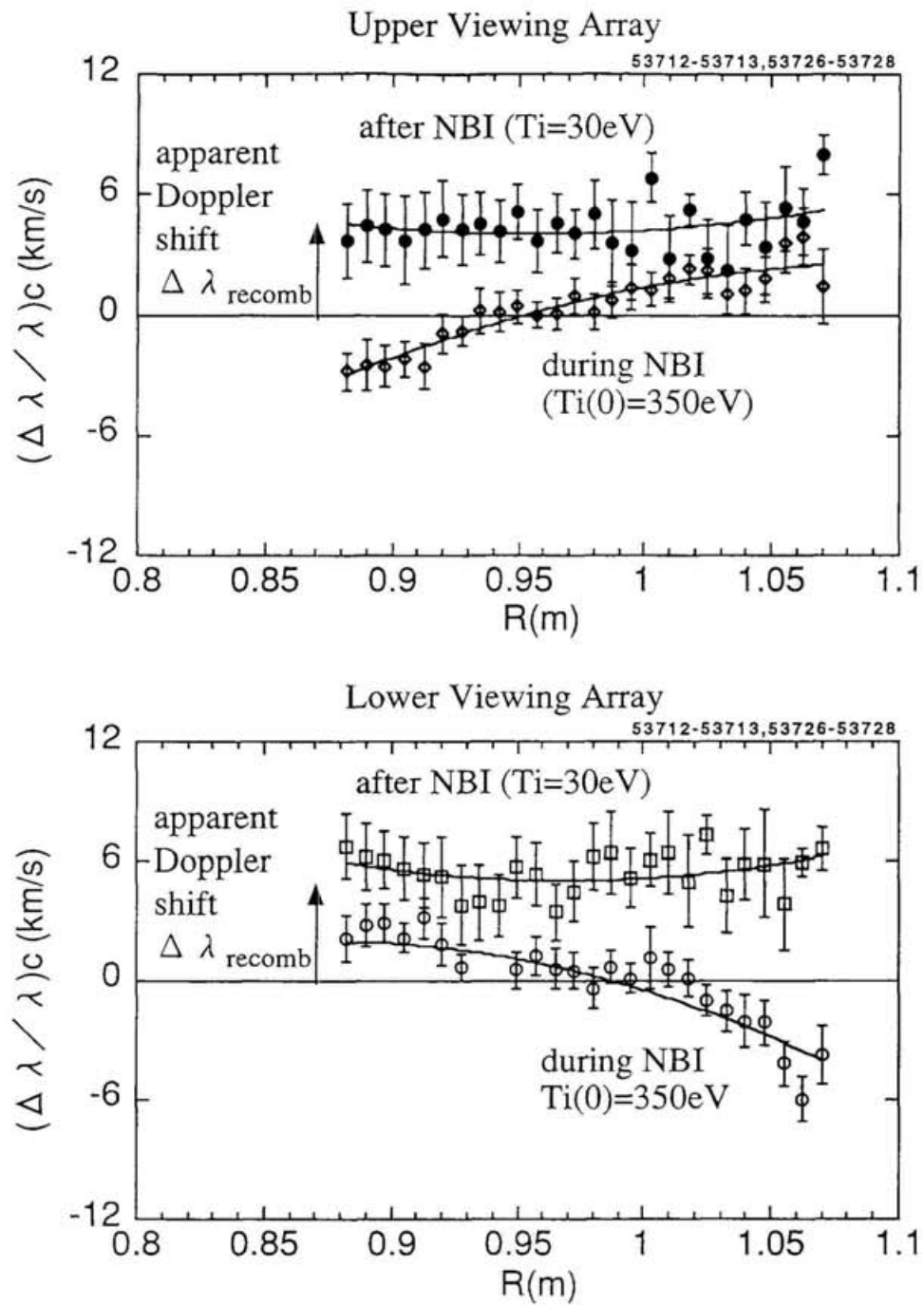


Fig.3.1.3.2 The wave length shifts in the NBI heated phase and the after-glow recombining phase. (CVI; $\Delta n=7-6$, $\lambda=3434 \text{ \AA}$)

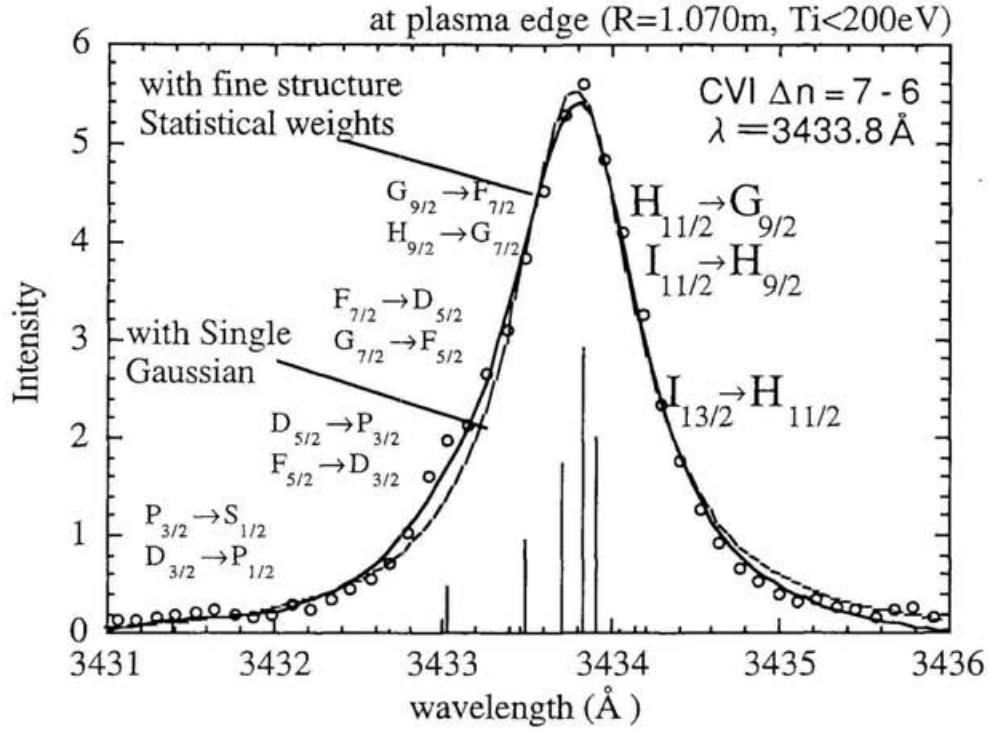


Fig.3.1.4: Spectral profile obtained at the plasma edge with the ion temperature of $< 200\text{eV}$, and the spectral fine structure pattern calculated using statistical weighted sub-level population. (CVI; $\Delta n=7-6$, $\lambda = 3434 \text{ \AA}$)

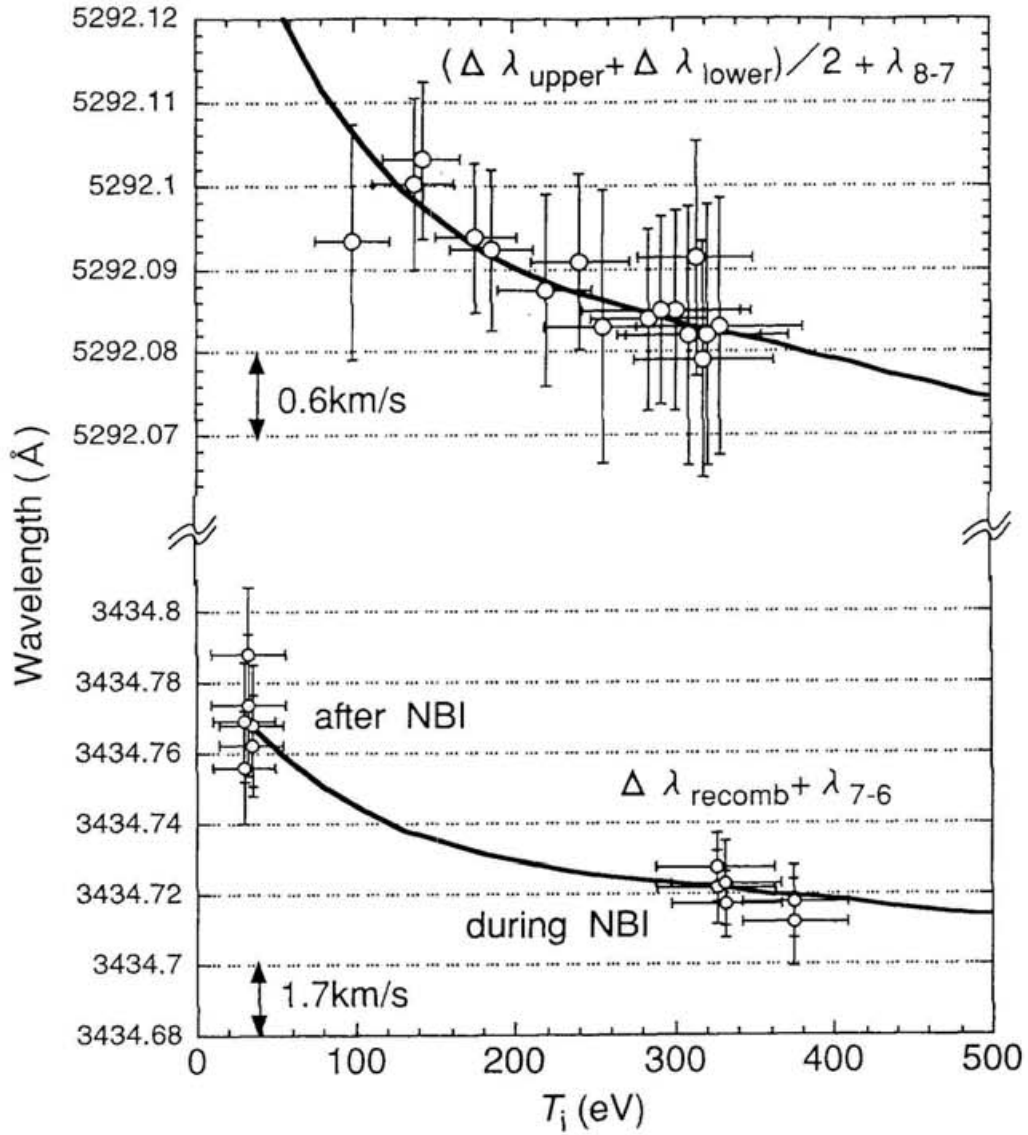


Fig.3.1.5: The dependence of the apparent wave length on ion temperature calculated for the CVI lines in visible range. (solid curve)
 And the measured 'apparent' wave length without 'real' Doppler shifts $(\Delta \lambda_{\text{upper}} + \Delta \lambda_{\text{lower}})/2 + \lambda_{8-7}$ from Fig.3 and the measured 'apparent' wave length $\Delta \lambda_{\text{recomb}} + \lambda_{7-6}$ in the after-glow recombining phase, where λ_{8-7} and λ_{7-6} are taken to be 5292.082 Å and 3434.72 Å respectively.

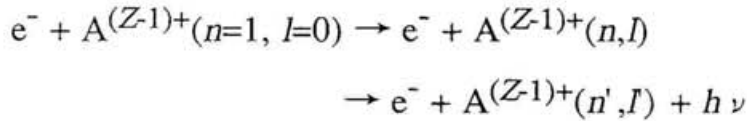
3.2 Background Radiation

To clarify the need and the validity of the use of reference channel to observing the background radiation mentioned in the previous chapter, the excitation process of this radiation is discussed here.

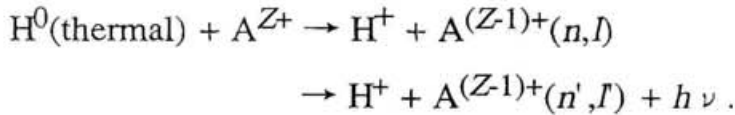
3.2.1 Effect of Cold Neutrals

The background radiation to the charge exchange spectral lines is observed in many devices and subtracting this cold spectral components is the one of the important technical issues in CXS. The dominant excitation processes are considered to be

(1) electron impact excitation expressed as



and/or (2) charge exchange with thermal neutral hydrogen atoms expressed as



In the charge exchange process of $H^0(\text{thermal})$ in the ground state ($n=1$), the cross sections into the excited states decrease with decreasing impact velocity and become negligible at the temperature of $T \sim 1\text{-}100\text{eV}$ when [34]. When $H^0(\text{thermal})$ is in the excited state ($n \geq 2$), however, the cross sections into the excited states of carbon are $\sim 10^{18}\text{cm}^{-2}$ even in the low temperature plasmas at the edge [35]. Therefore this charge exchange excitation is not negligible if the density of thermal neutrals in excited

states is comparable to that of the beam neutrals in the ground state. The toroidal symmetry or the toroidal periodicity of the background radiation, which is assumed in the use of the reference channel, may break down when this excitation process is dominant. Therefore the toroidal periodicity of the background radiation should be confirmed in various operating conditions. Thermal neutrals are (1) generated by the plasma-wall interaction, (2) injected from the NB injector, (3) injected from the gas puffing port, or (4) generated by the NB-wall interaction, and may have poloidally and toroidally non-uniform distribution. Although the experiment to measure the inside/outside asymmetry of poloidal flows are done without gas puffing or with weak gas puffing because of the need for low electron density described in section 3.3, the effect of these non-uniform neutrals on the toroidal periodicity of the background radiation was examined by following methods in the plasmas sustained only by NBI#2 or ECH (without NBI#1).

- (1) The comparison of the intensities at the port viewing the NB#1 and at the port viewing the background(the reference channel) to check the toroidal non-periodicity of the plasma-wall interaction.
- (2) Investigating the change of the intensities corresponding to the opening/closing of gate-valve at the NBI#1 injection port to check the effect of neutrals injected from the NB injector. At this time, the ion source in NB injector#1 is active but the accelerating voltage is switched off.
- (3) Investigating the intensities in gas-puffed discharge and not gas-puffed discharge.

Figure 3.2.1 shows the intensities of the CVI line in the plasmas sustained only by NBI#2. The intensities are given by the least square fitting of multiple Gaussian curve described in the previous section. In the both of the discharges with $R_{ax}=92.1\text{cm}$ and $R_{ax}=97.4\text{cm}$, the intensity profiles observed at 7U/7D ports and that at 8D port(the reference channel) are almost identical irrespective of the neutrals injected from the

NB injector#1. Figure 3.2.2 shows the CVI line intensity profiles observed in ECH plasmas with and without gas-puffing. The intensity profiles observed at the 7U/7D port and that at the 8D port are also almost identical in these plasmas.

Another important characteristic of the background CVI radiation in CHS is that the radial profile of the intensity is rather flat as shown in Figure 3.2.1 and Figure 3.2.2 while the H_α intensity profile has the strong inside/outside asymmetry (larger than factor 2 at $\rho \sim 0.9$) as shown in Figure 3.2.3. The plasmas touch the inner wall of the vacuum vessel or are situated near to the wall as shown in Figure 1.2 and Figure 1.3. This strong inside/outside asymmetry of H_α intensity indicates the inside/outside asymmetric neutral density profile due to the strong neutral flux from the inner wall. The flat intensity profile of the background CVI radiation indicates that it is not caused by the charge exchange with thermal neutrals, but caused by the electron impact excitation.

The spectral profile and the intensity of H_α shown in Figure 3.2.3 indicate also the difficulty of the CXS measurement of the bulk ion itself mentioned in Chapter 2.

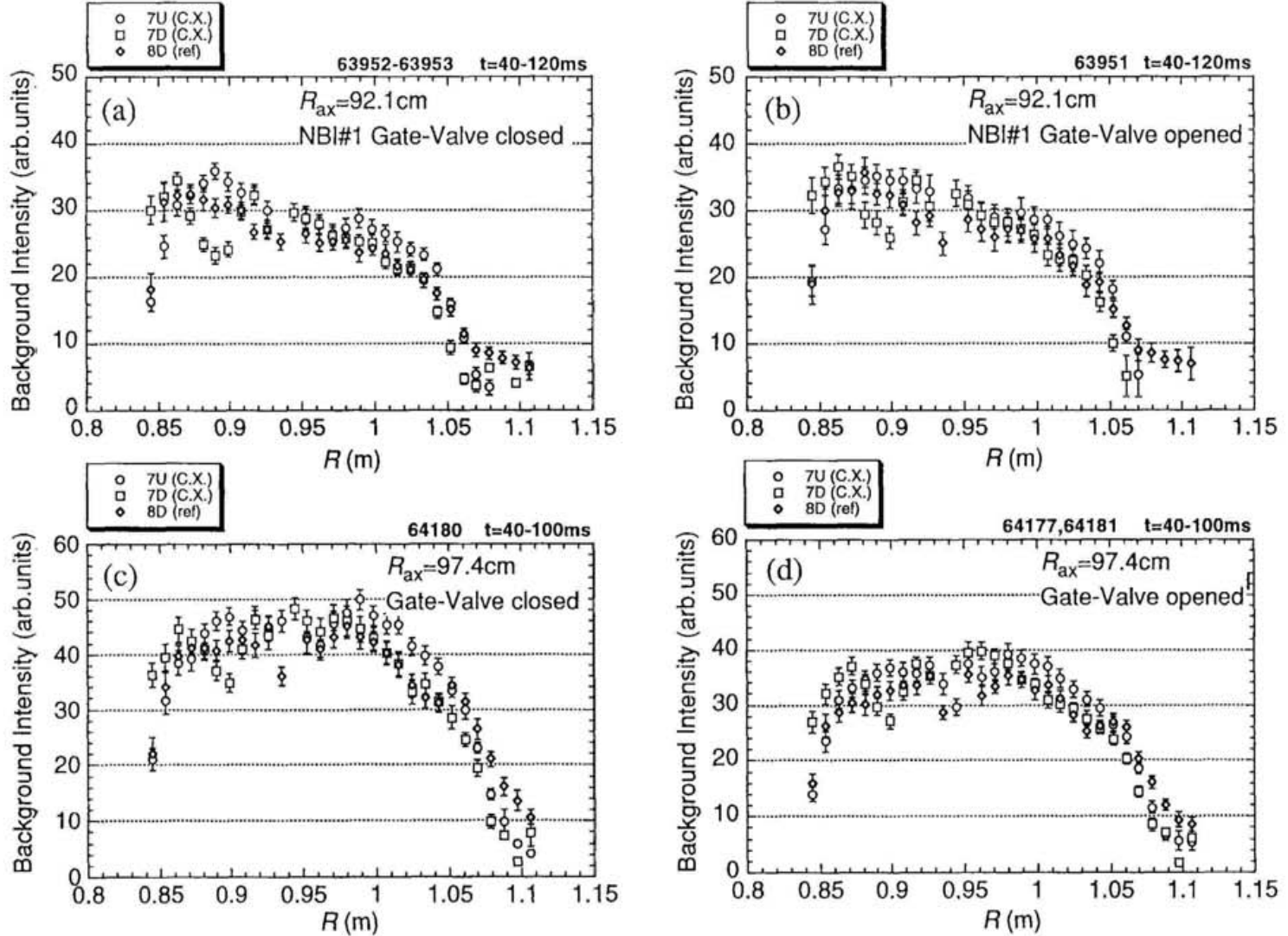


Figure 3.2.1 The intensity of the CVI line observed in the plasmas sustained only by NBI#2 (without the charge exchange with NB#1). In the both of the discharges with $R_{ax}=92.1$ and $R_{ax}=97.4\text{cm}$, the intensity profiles observed at 7U/7D(viewing NB#1) port and that at 8D port(the background reference channel) are same irrespective of the neutrals injected from the NB injector#1. (a)(b) $R_{ax}=92.1\text{cm}$, $B_t=1.2\text{T(CW)}$, $\bar{n}_e \sim 1 \times 10^{13}\text{cm}^{-3}$, w/o Gas-Puff. (c)(d) $R_{ax}=97.4\text{cm}$, $B_t=1.5\text{T(CCW)}$, $\bar{n}_e \sim 1 \times 10^{13}\text{cm}^{-3}$, w/o Gas-Puff.

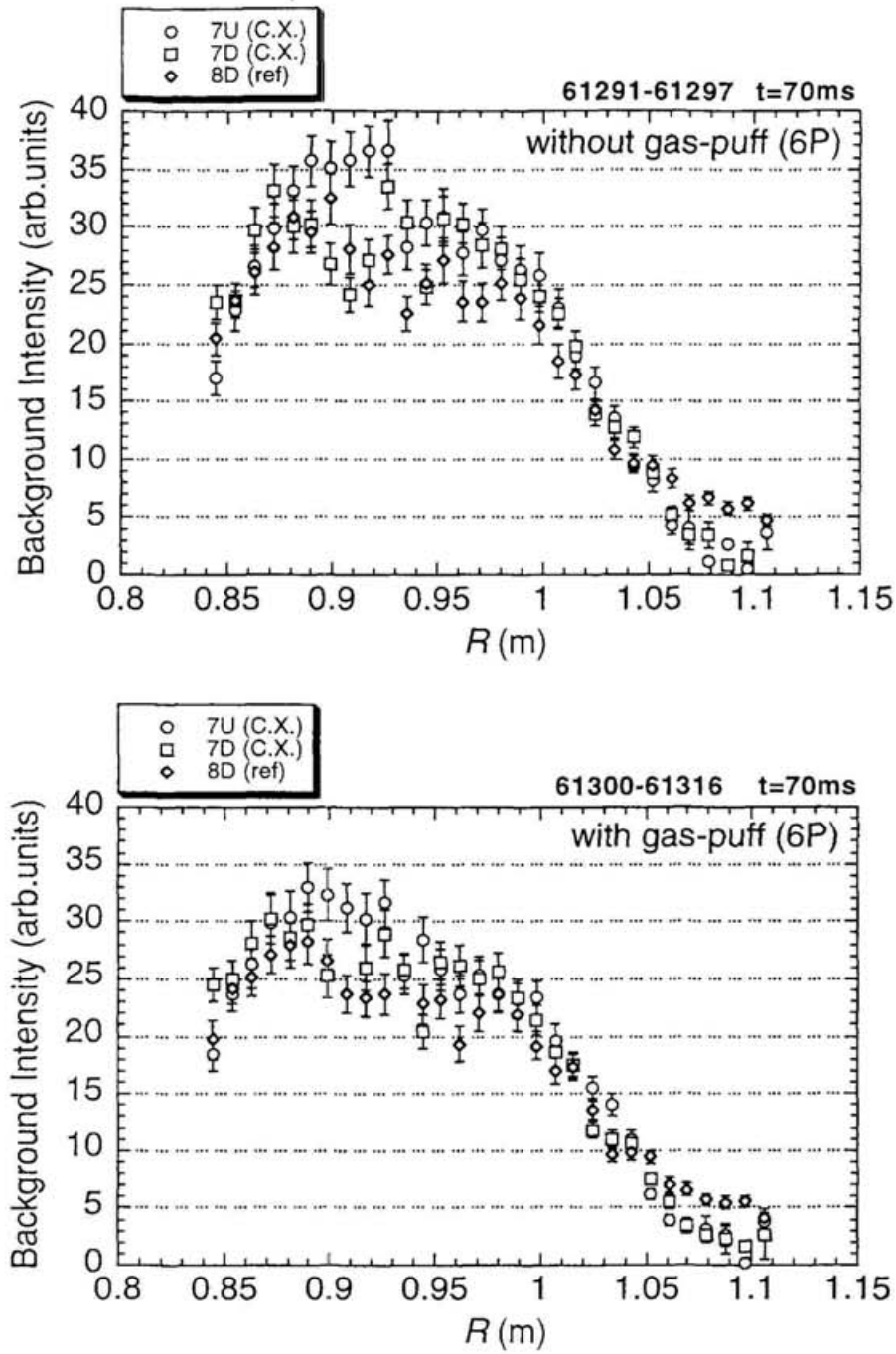


Figure 3.2.2 The CVI line intensity profiles observed in ECH plasmas with and without gas-puffing . The intensity profiles observed at 7U/7D port and that at 8D port are also same in these plasmas.

(a) The intensity in ECH plasma without gas-puffing.

$$R_{ax}=92.1\text{cm}, B_t=1.7\text{T(CCW)}, \bar{n}_e<0.5\times 10^{13}\text{cm}^{-3}.$$

(b) The intensity in ECH plasma with gas-puffing.

$$R_{ax}=92.1\text{cm}, B_t=1.7\text{T(CCW)}, \bar{n}_e\sim 1.5\times 10^{13}\text{cm}^{-3}.$$

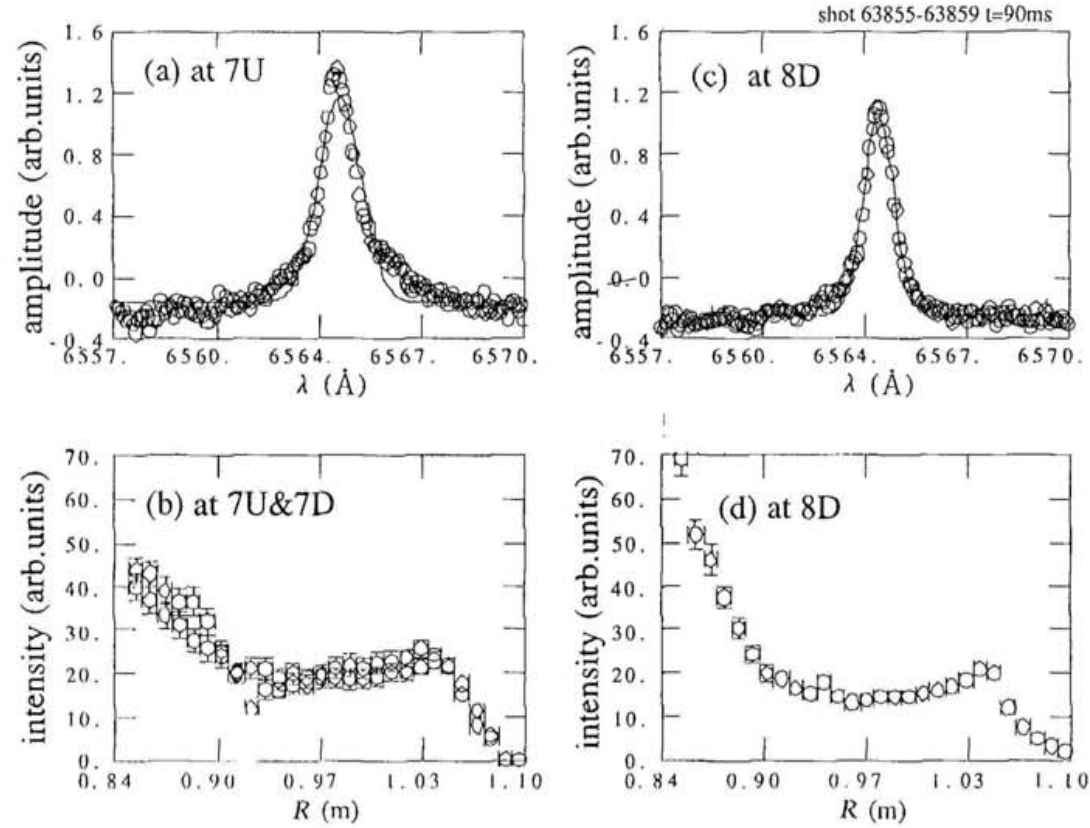


Figure 3.2.3 The spectral profile and intensity of $H\alpha$ line observed in NBI#1 heated H-plasma with the condition of $R_{ax}=92.1$ cm, $B_t=1.7$ T(CCW), $n_e=1.8\times 10^{13}\text{cm}^{-3}$.

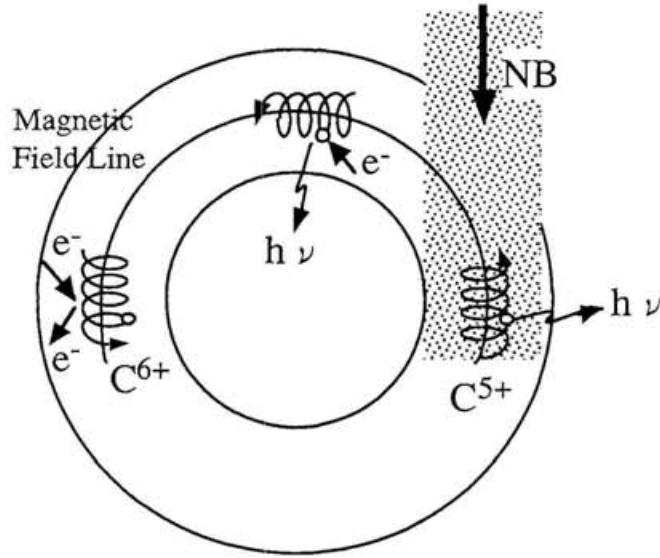
The charge exchange hot spectrum component at port 7U/7D (viewing the beam) due to the beam is almost masked by the cold component. This spectrum also includes the radiation from the beam itself. The strong inside/outside asymmetry of background intensity is caused by the neutral flux from the inner wall

(a) spectrum at 7U (at $R=0.97$ m), (b) intensity at 7U/7D,

(c) spectrum at 8D (at $R=0.97$ m), (d) intensity at 8D (background reference channel)

3.2.2 Plumbing Effect

The radial profiles of the intensities of the background CVI radiation in CHS are toroidally periodic and rather inside/outside symmetric compared with the H_{α} intensity profiles as described above. The magnitude and the profile of the intensity can be explained using the "plume" model[29]



$$\text{mean free path} \sim \frac{V_{\text{thi}}}{n_e \langle \sigma v \rangle_e^{\text{ionize}}} \sim 80\text{m}$$

(at $T_e \sim 400\text{eV}$, $T_i \sim 200\text{eV}$, $n_e \sim 10^{13}\text{cm}^{-3}$)

Figure3.2.4 The concept of "plume". The ionization mean free path of C^{5+} ion in CHS plasma parameter regime is larger than the plasma dimension.

Figure 3.2.4 shows the concept of "plume". The lifetime of excited states of charge exchange product $A^{(Z-1)+}$ ions are short (for example, it is 5.3×10^{-10} sec for the $n=8$ state of C^{5+}). Thus the radiation due to the beam charge exchange ("prompt" radiation) occurs at the position where the charge exchange occurs. After these radiative transition, however, the ionization of product ions need not so short time. In the typical NBI plasmas in CHS ($T_e \sim 400$ eV, $T_i \sim 200$ eV, $n_e \sim 10^{13} \text{ cm}^{-3}$), the mean free path of the electron impact ionization of C^{5+} is about 80 m. Thus the density of the NB produced C^{5+} ions can be considered as the surface quantity. The "plume" is the charge exchange product $A^{(Z-1)+}$ ion which causes the radiation due to electron impact excitation before electron impact ionization[29]. In the case of the long ionization mean free paths as like C^{5+} in CHS, the "plume"- "prompt" intensity ratio is estimated as

$$\frac{I_{\text{plume}}}{I_{\text{C.X.}}} \sim \frac{\langle \sigma v \rangle_{\text{C.X.}}^{\text{total}}}{\langle \sigma v \rangle_{\text{C.X.}}^{\text{excite}}} \cdot \frac{\langle \sigma v \rangle_e^{\text{excite}}}{\langle \sigma v \rangle_e^{\text{ionize}}} \quad (3.2.1)$$

where $\langle \sigma v \rangle_{\text{C.X.}}^{\text{excite}}$ and $\langle \sigma v \rangle_{\text{C.X.}}^{\text{total}}$ are the partial rate coefficient into the excited states and the total rate coefficient of charge exchange, and $\langle \sigma v \rangle_e^{\text{excite}}$ and $\langle \sigma v \rangle_e^{\text{ionize}}$ are the excitation rate coefficient into the states and the ionization rate coefficient of electron impact, respectively.

Under the condition of $E_b \gg T_i$, where E_b is the beam energy, the ratio

$\langle \sigma v \rangle_{\text{C.X.}}^{\text{total}} / \langle \sigma v \rangle_{\text{C.X.}}^{\text{excite}} = \sigma_{\text{C.X.}}^{\text{total}} / \sigma_{\text{C.X.}}^{\text{excite}}$ is the function of beam energy only and thus is considered to be a constant in our experiments. These cross sections for charge exchange reactions are listed in Ref[34]. $\langle \sigma v \rangle_e^{\text{excite}}$, $\langle \sigma v \rangle_e^{\text{ionize}}$ and their ratio $\langle \sigma v \rangle_e^{\text{excite}} / \langle \sigma v \rangle_e^{\text{ionize}}$ is the function of electron temperature as shown in

Figure 3.2.5[36,37], and Figure3.2.6. Under the condition with the beam energy of $E_b \sim 40\text{keV}$ and the electron temperature of $T_e \sim 400\text{eV}$, this ratio is $I_{\text{plume}}/I_{\text{C.X.}} \sim 1$ and thus the observed strong background intensity comparable to the intensity of "prompt " radiation due to the beam can be explained as this pluming effect. Figure 3.2.7 shows an example of the intensity profile of the charge exchange spectral line after subtracting background and the background CVI line, and the electron temperature profile measured with YAG Thomson scattering in this discharge.

The relation (3.2.1) expresses the characteristics of "plume"-"prompt" ratio that depends mainly on the electron temperature, under the approximation that neglects the l-mixing process, the cascade transitions from the upper levels and the ladder-like excitation from lower levels. The intensity profile of the background radiation in Figure 3.2.7 can be discussed qualitatively using this dependence. The intensity profile of "plume" calculated from this production profile (i.e. "prompt" intensity profile) on the outside of the magnetic axis using the relation

$$I_{\text{plume}}/I_{\text{C.X.}} \propto \langle \sigma v \rangle_e^{\text{excite}} / \langle \sigma v \rangle_e^{\text{ionize}}$$

in this discharge is shown in Figure3.2.8. The Abel inversion[38] of the observed background radiation also is shown with the solid line with the mark \bigcirc . Both of the calculated profile and the Abel inverted observed profile of the background intensity are the hollow profiles which have the peak at $\rho = \rho_{\text{peak}} \sim 0.8$. In corona equilibrium calculation, ρ_{peak} will only depend on electron temperature[39].The observed intensity profiles, however, do not show this dependence, but show the profile determined by the balance of NB charge exchange and electron impact ionization.

Thus the magnitude and the radial profile of background CVI intensity in the plasma parameter regime of NBI heated CHS plasmas can be explained using the "plume" model. The density of C^{5+} can be considered as the surface quantity because of the long mean free path of electron impact ionization. It can explain that the observed background CVI

intensity profiles are toroidally periodic and rather flat compared with the poloidally non-uniform H_α intensity.

The Doppler shifts of this background CVI spectral lines due to electron impact excitation does not express the rotation velocity of fully ionized A^{Z+} ions. The velocity obtained from these Doppler shifts includes the diamagnetic drift velocities of hydrogen-like incompletely ionized $A^{(Z-1)+}$ ions. The direction of this drift is the direction of the electron diamagnetic drift at $\rho < \rho_{\text{peak}}$ and differ from that of fully ionized A^{Z+} ions[40]. Figure 3.2.8 shows the Doppler shifts of the CVI line in the discharge described in section 3.1.2. These shifts are given by the non-linear least square fitting of the multiple Gaussian curve. The Doppler shift of the charge exchange radiation observed at 7D port and that of background radiation at 8D port differ from each other in magnitude and spatial distribution profile. This difference indicates the drift velocity difference between the ionization states of impurity ions. This is one of the important reason of using the reference channel. In order to obtain the rotation velocity (not only the density) of fully ionized A^{Z+} ions, the background spectrum should be subtracted even in peripheral region where double Gaussian fitting is not effective because of the narrow Doppler broadening of the NB charge exchange spectral line.

It may be noted that the beam modulation technique is not appropriate when the "plume" is the dominant process of background radiation since the modulation should be faster than the ionization time ($\sim 1\text{kHz}$) to avoid the modulation of the background itself. Such a fast modulation of the beam and the synchronous detection are impossible in the system described in Chapter 2. The optimization of beam modulation speed is the future theme of the diagnostics neutral beam experiments in CHS[41]

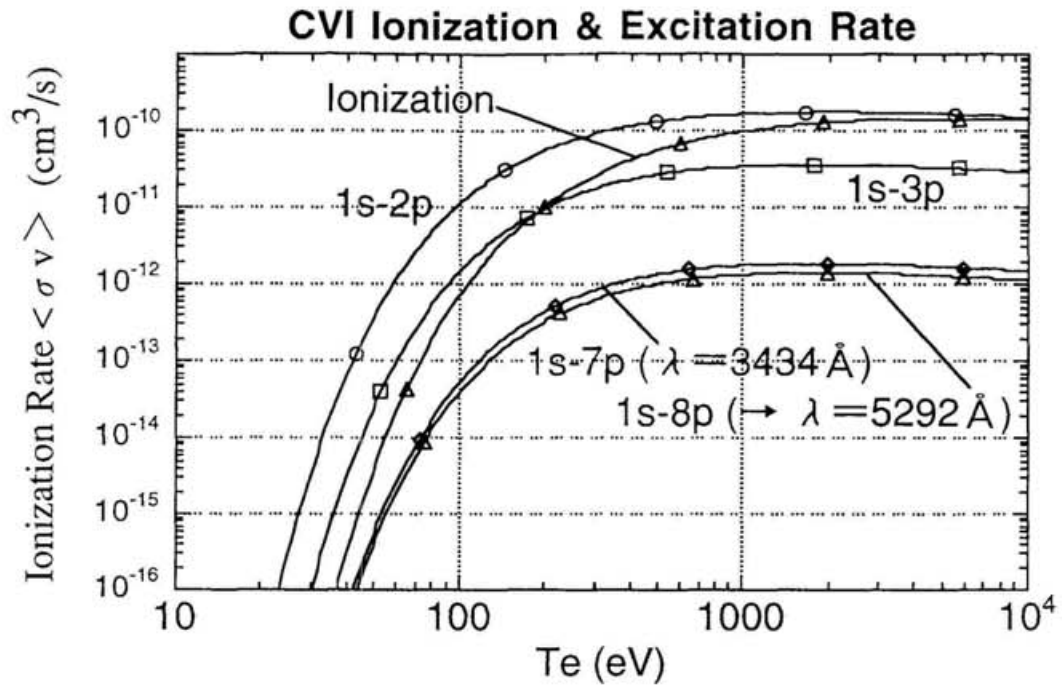


Figure 3.2.5 The electron impact excitation and ionization rate coefficients of C^{6+} ion calculated from the Tables in Ref[36] and Ref[37].

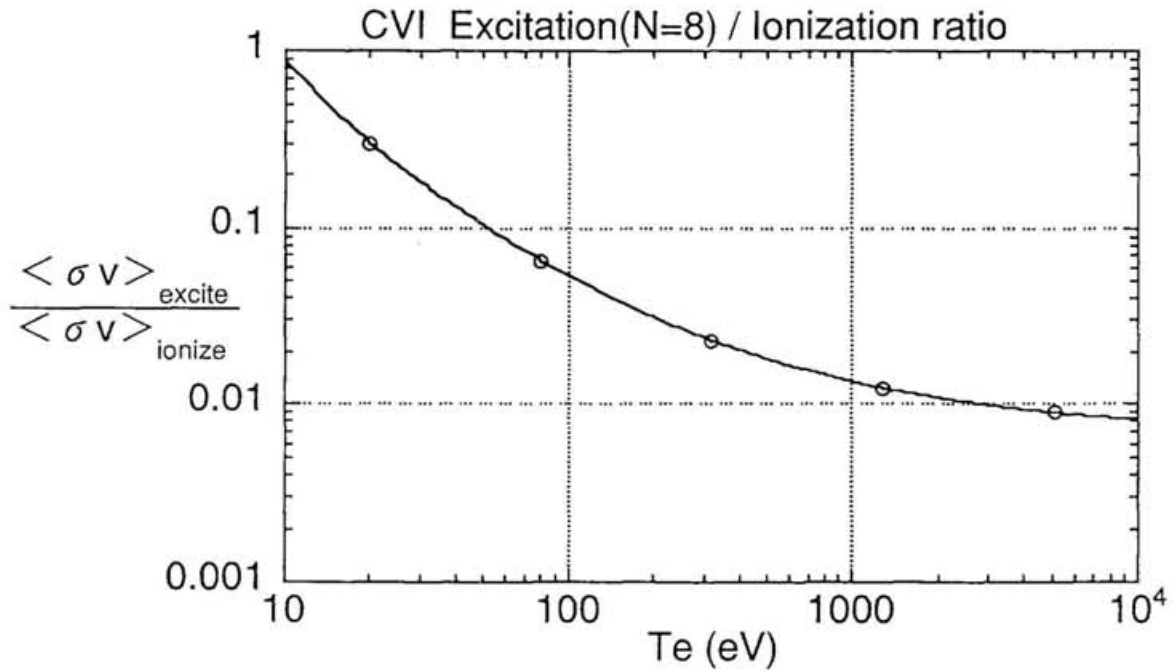


Figure 3.2.6 The ratio of the excitation rate to the ionization rate.

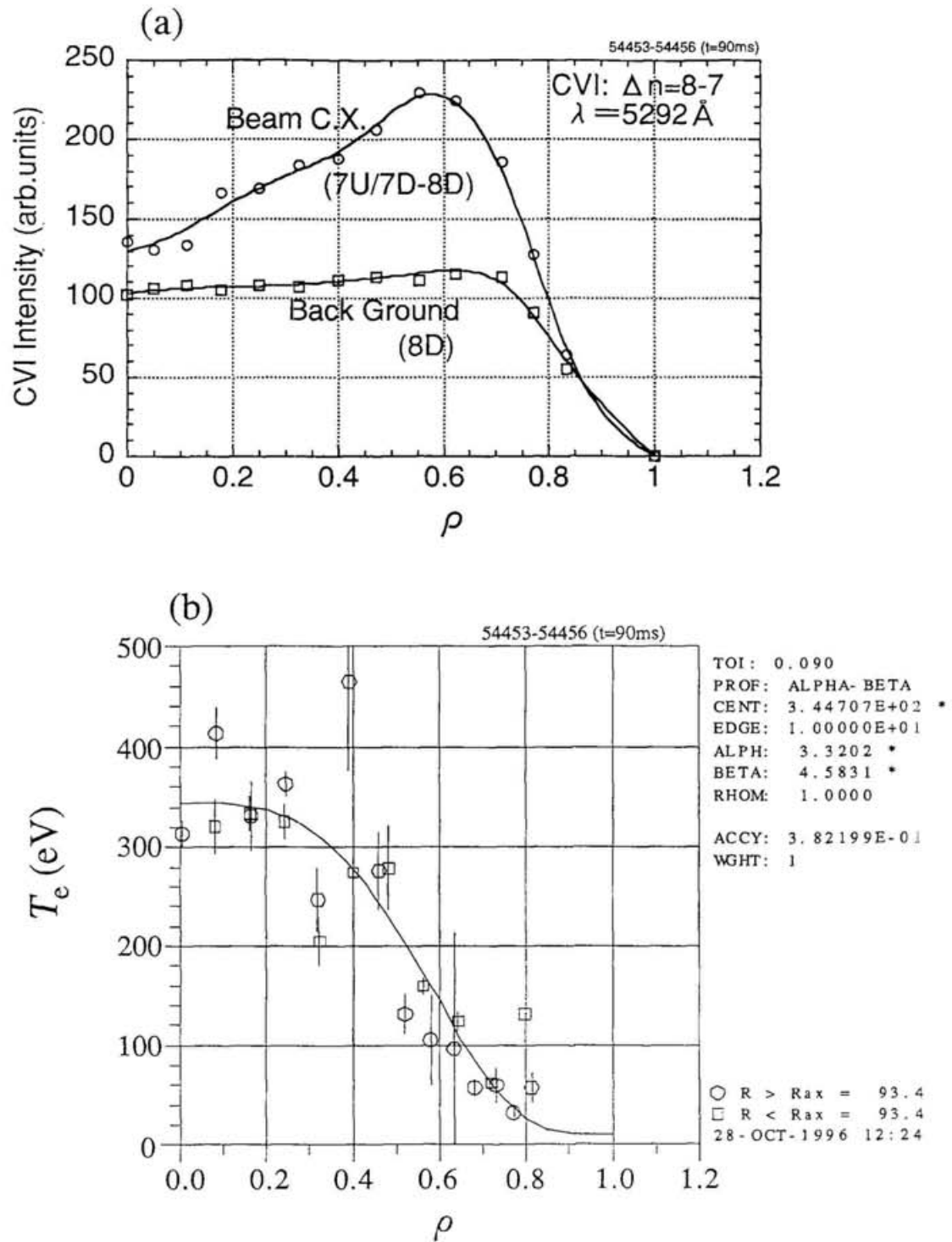


Figure 3.2.7 The example of (a) the intensity profile of the charge exchange spectral line (after subtracting background) and the background CVI line, and (b) the electron temperature profile in this discharge, for the "plume" model calculation.

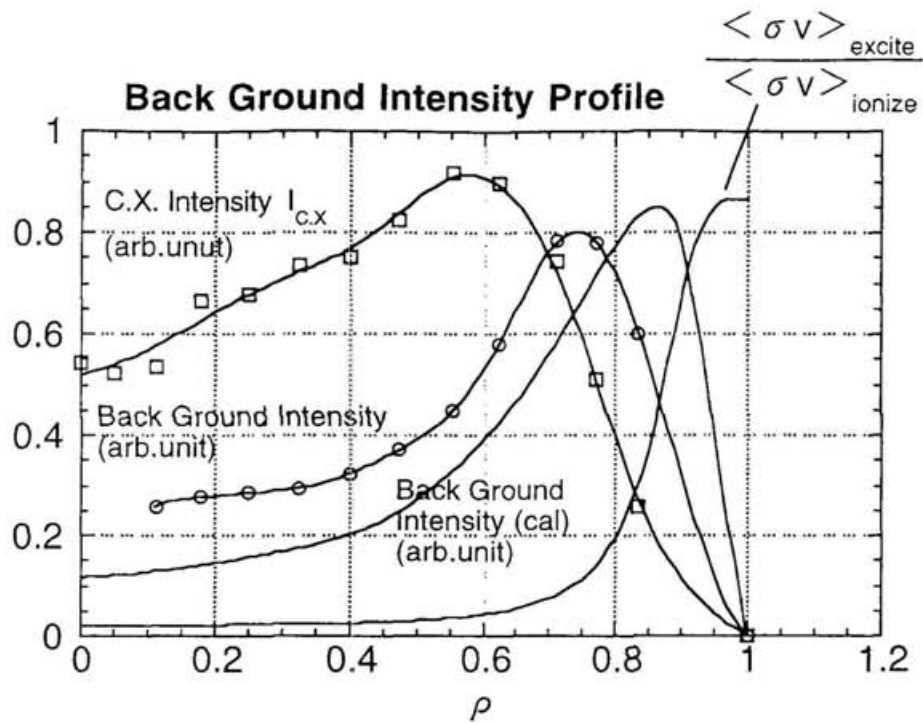


Figure 3.2.8 The comparison of the Abel converted observed background intensity profile (line with \circ) and the profile calculated from the charge exchange spectral intensity $I_{c.x.}$ with "plume" assumption (solid line). $I_{c.x.}$ is also shown by \square . These intensities are normalized individually for the comparison.

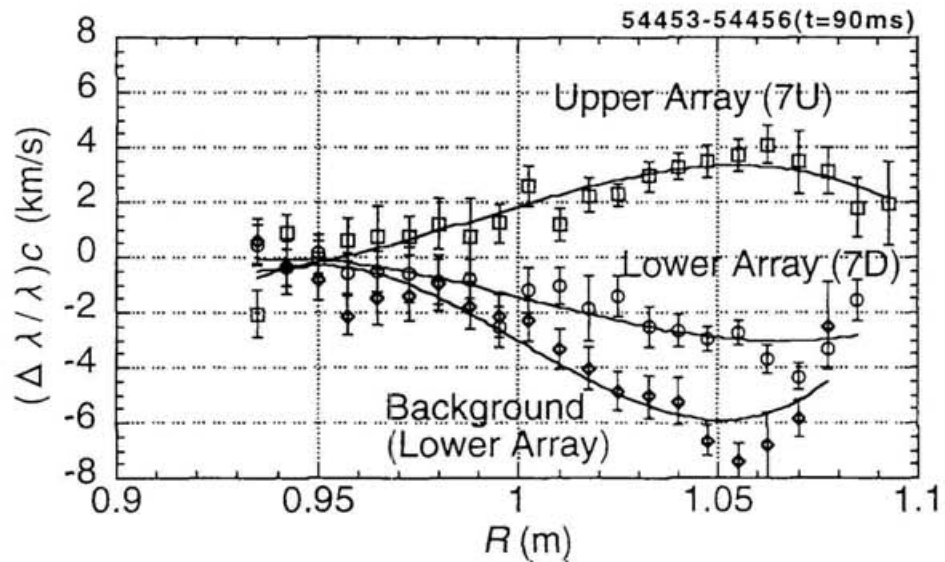


Figure 3.2.9 The Doppler shifts of the CVI line ($\lambda = 5290 \text{ \AA}$) in the discharge described in section 3.1.2 after correcting the the apparent shift due to the fine structure. The difference between charge exchange radiation and the background radiation expresses the drift velocity difference between ionization states.

3.3 Neutral Beam Density

3.3.1 Measurements of the Initial Density Profile

In order to investigate the flow conservation, the density profiles of the fully ionized carbon ions were measured using the intensity of the charge exchange spectral lines. For this purpose, the initial beam density profile without attenuation in plasmas was also measured in the torus using H_α from the beam. Of course this kind of measurements (i.e. the measurements of the beam divergence angle, the beam focusing point and injection angle) had been done already in the neutral beam injector itself, however, the measurement in the torus, which attain the accuracy of density profile enough to discuss the poloidal flow conservation at the vertical elongated section where the CXS measurements are done, has never been done. For this measurement, the neutral beam was injected into the torus without the target plasma and the magnetic field ($B=0T$) and the H_α emission from the beam was observed. The H_α spectrum and the intensity profile measured at the vertically elongated section (port 7U and 7D) are shown in Figure 3.3.1 and Figure 3.3.2 respectively. The negligibly small intensity at the background reference channel (port 8D) indicates that there are no plasmas emitting H_α line. The spectrum observed at port 7U and 7D have a 'cold' component emitted from cold neutral gas with the temperature of $T \sim 1eV$ generated by the beam-wall interaction and/or released from NB injector. This cold component is separated using the nonlinear least square double Gaussian fitting. The intensity ratio of the 'cold' component and the 'hot' component indicates that the density of the cold neutral atoms in the excited states is negligibly small compared with the density of the beam neutral atoms in the ground state. Therefore the effect of the cold neutral gas generated by the beam-wall interaction on the background intensity mentioned in the previous section is considered to be negligible.

The hot component emitted from the beam has a Doppler broadening corresponding to the beam divergence angle $\text{HWHM}/\lambda_{\alpha} \times c/v_b = 1.4 \pm 0.2^\circ$ as shown in Figure 3.3.3, where λ_{α} , c and v_b are the wavelength of $H\alpha$, the velocity of light and the velocity of the beam, respectively. This broadening includes the effect of staring angle thus has a peaking profile.

This $H\alpha$ intensity profile expresses the chord integrated density profile of the beam. The solid line in the Figure 3.3.2 is the density profile calculated using the design value (or the value measured in the NB injector) of the beam divergence angle, the beam focusing point and injection angle. The discrepancy is considered to be the errors of these parameters since the precise measurements of these parameters need the longer distance between the ion source and the observed point, so a beam deposition profile measurement using the calorimeter in the torus is planned in the near future.

The measured intensity includes the emission from the first, the second and the third energy components with the energy of E_b , $E_b/2$, and $E_b/3$, where E_b is the accelerating voltage. The density ratio of these components is $n_{1/1}:n_{1/2}:n_{1/3} = 0.6:0.1:0.3$. In the CXS measurements using the CVI lines, the emission caused by the second and/or the third energy components is negligible[29]. Therefore, only the density of the first energy component is discussed from next section. In these beam attenuation calculations, the initial density profile of the first energy component is assumed to be proportional to the $H\alpha$ intensity profile measured here.

3.3.2 Beam Attenuation

The dominant beam ionization processes in the plasmas are considered to be [42] (1) charge exchange with protons, (2) proton impact ionization and (3) electron impact ionization.

The configuration of beam injection is shown in Figure 3.3.4. The beam diameter near the injection port at a horizontally elongated section is smaller than plasma minor radius and it becomes comparable to the plasma dimension near the vertically elongated section where the CXS measurements are done. The characteristic length with which the plasma parameters change in vertical direction at this vertically elongated section is large compared with the beam diameter shown in Figure 3.3.2. Therefore, the beam attenuation calculation to obtain the beam density profile integrated along the viewing chords can be done with the plasma parameters at the mid-plane ($Z=0$ plane) using the equation

$$n_b(R, \phi) = \exp\left[- \int \sum_a n_a \langle \sigma v \rangle_a / v_b dl\right] n_b(\text{initial}) \quad (3.3.1)$$

where $n_b(R, \phi)$, $n_b(\text{initial})$, v_b and l are the attenuated beam density at position with major radius of R and the toroidal angle of ϕ , the initial density at this position, beam velocity, and the distance along the beam between this position and the plasma edge.

The ionization rate $\sum_a n_a \langle \sigma v \rangle_a$ can be calculated with the approximation

$$\begin{aligned} & \sum_a n_a \langle \sigma v \rangle_a \\ & \equiv n_e(\rho) \langle \sigma_e v \rangle + n_p(\rho) \langle (\sigma_p + \sigma_{cx}) v \rangle \\ & \cong n_e(\rho) (\langle \sigma_e v \rangle + (\sigma_p + \sigma_{cx}) v_b) \end{aligned}$$

where $n_e(\rho)$, $n_p(\rho)$, σ_e , σ_p , σ_{cx} , are the densities of electrons and bulk ions, and the cross sections for electron impact ionization, proton/deuterium impact ionization, charge exchange with proton/deuterium, respectively, and the rate coefficients $\langle \sigma v \rangle$ are the average of the products of these cross sections and the relative impact velocities. σ_p , σ_{cx} and $\langle \sigma_e v \rangle$ are given in Ref[42]. This ionization rate is the function of the density and temperature of electron and can be calculated using the density and temperature profiles of the electron measured with YAG Thosom scattering and HCN laser interferometer. The integration of this function are done numerically on the magnetic surfaces(Figure 3.3.4) calculated with the finite- β 3-D equilibrium code VMEC[43].

The example of calculated beam density profiles in the plasmas is shown in Figure 3.3.5. The magnetic axis position and the density and temperature profiles of electrons are assumed to be $R_{ax}=99.5\text{cm}$, $n_e(\rho)[\text{cm}^{-3}]=2.0 \times 10^{13} \times [1 - \rho^{7.4}]^{1.4} + 1.0 \times 10^{12}$, and $T_e(\rho)[\text{eV}]=200.0 \times [1 - \rho^{1.9}]^{2.3} + 10.0$, respectively.

This condition corresponds to that of the discharge shown later in Chapter 4 . In these low density region, the beam density at $\rho \sim -0.5$ is still larger than the half of that at $\rho \sim +0.5$ and changes only $\pm 10\%$ even when the electron density is changed $\pm 20\%$. This indicates that we can measure the parameters(the ion temperature T_i , the poloidal rotation velocity V_p and the density of fully ionized impurity n_i) on the inside of magnetic axis using CXS.

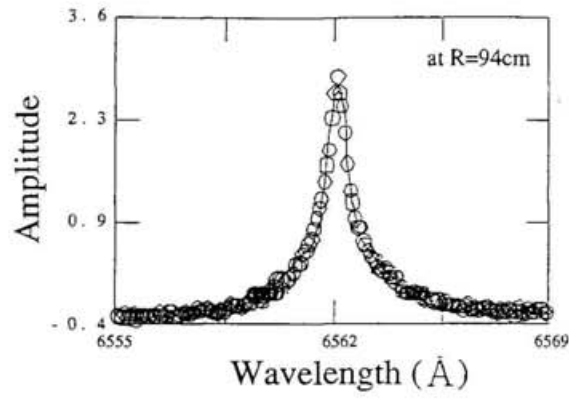


Figure 3.3.1 H_{α} spectrum of the beam

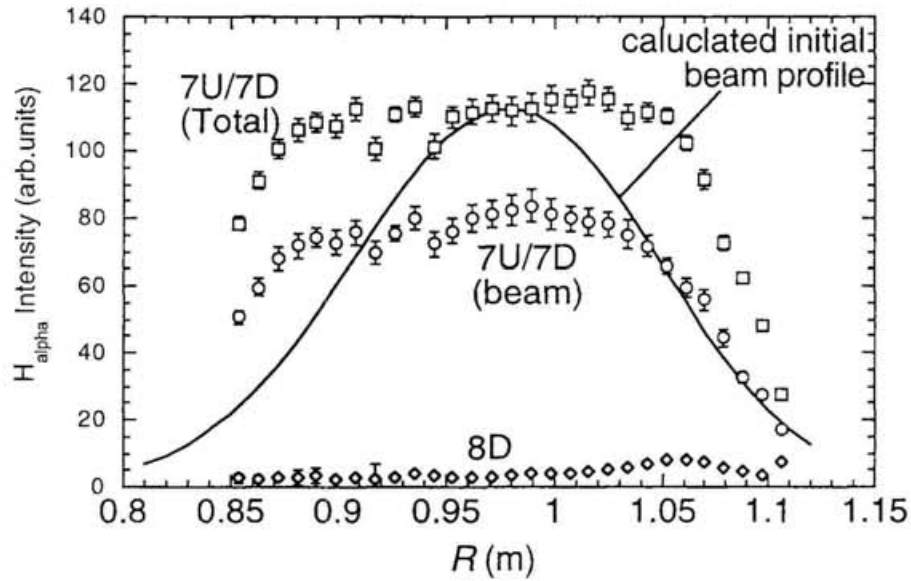


Figure 3.3.2 The spatial distribution profile of H_{α} intensity of the beam at the vertically elongated sections in the condition of the accelerating voltage of $E_b=38\text{kV}$.

The cold component of the spectrum at the port 7D/7U is separated with a double Gaussian fitting, so both of the total intensity and the intensity of the hot component (beam component) are shown.

The calculated initial beam density profile is also shown.

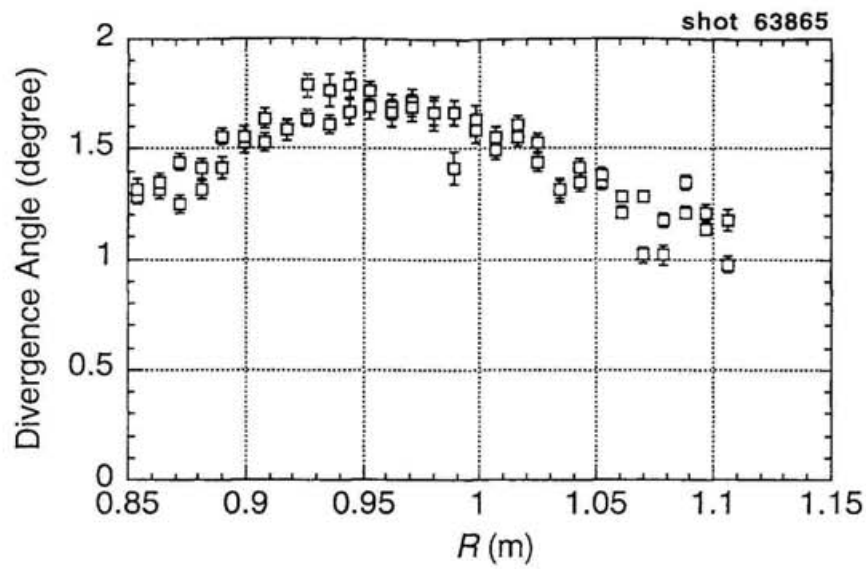


Figure 3.3.3 The divergence angle obtained from the Doppler broadening of the H_{α} from the beam. This broadening includes the effect of staring angle thus has a peaking profile.

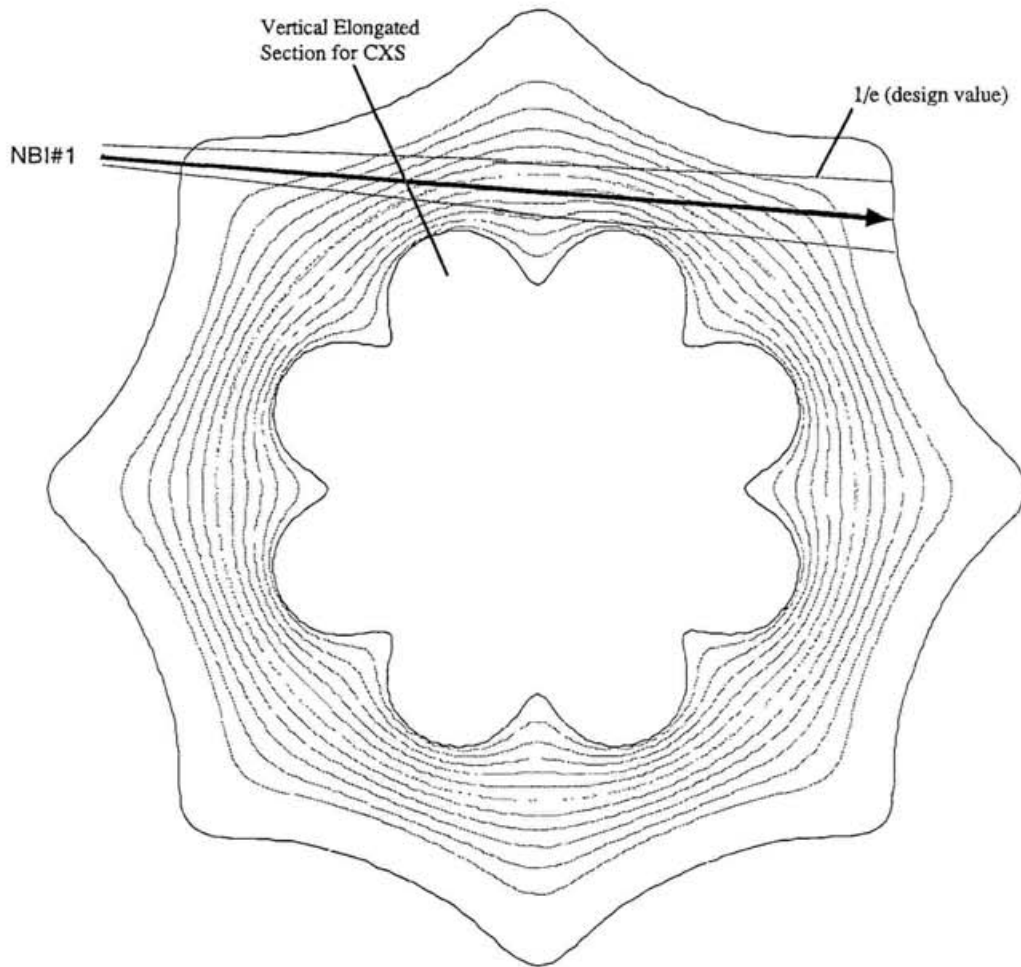


Figure 3.3.4 The configuration of beam injection.
The magnetic surfaces is the example for the configuration of $R_{ax}=92.1\text{cm}/\beta=0\%$

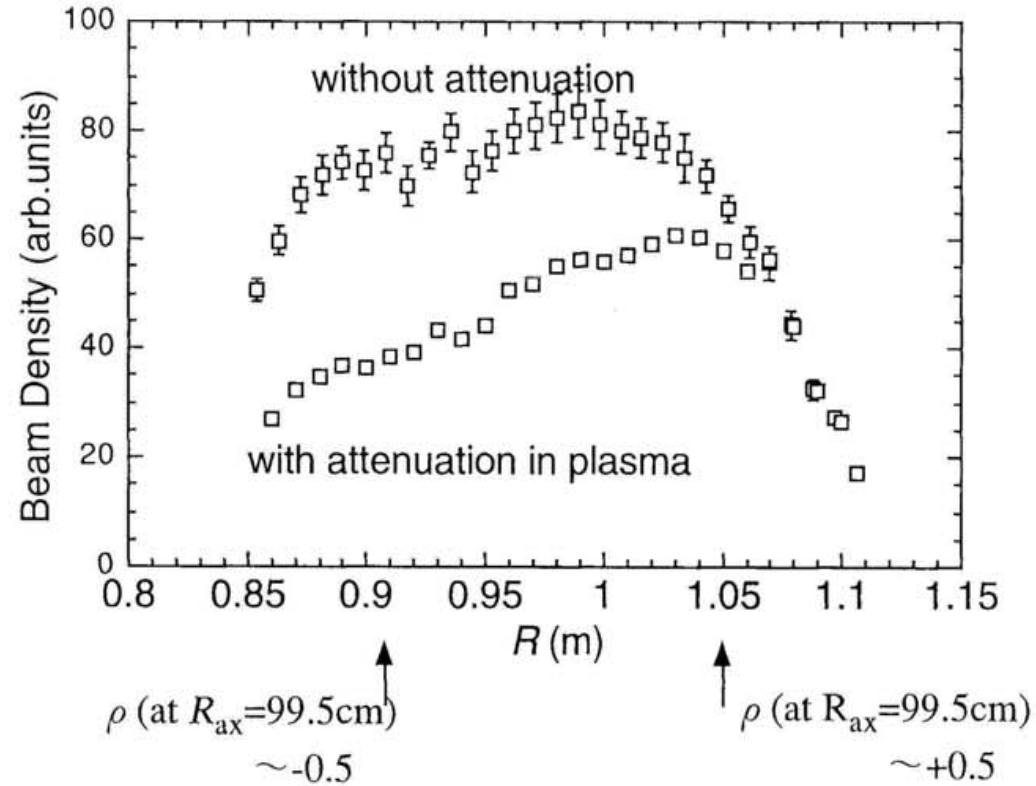


Figure 3.3.5 Comparizon of the initial beam density profile without attenuation and the example of the beam density profile attenuated in the plasma. The attenuation was calculated with the condition of the discharge described in Chapter 4
 $(R_{ax}=99.5\text{cm}, T_e(0)=200\text{eV}, n_e = 1.7 \times 10^{13}\text{cm}^{-3})$

Chapter 4

Poloidal Flow Measurement Results and Discussions

4.1 Measured Velocity and Density Profiles

The measurements of the rotation velocities and the densities were done in the condition with low line averaged electron density ($n_e < 2 \times 10^{13} \text{cm}^{-3}$) to avoid the ambiguity of beam attenuation calculation and the degradation of signal level on the inside.

Figure 4.1.1 shows the examples of the Doppler shifts of CVI line ($\Delta n=8-7$, $\lambda=5290 \text{\AA}$) at the vertically elongated section in the configurations of $R_{ax}=92.1 \text{cm}$ and $R_{ax}=99.5 \text{cm}$ where R_{ax} is the major radius of the vacuum magnetic axis. In the inward shifted ($R_{ax}=92.1 \text{cm}$) configuration, the gradients of surface function ($d\Psi/dR$), which determine the strength of the radial electric fields, on the inner side and the outer side of the section are almost symmetric, and thus the Doppler shifts on both sides were also almost symmetric. On the contrary, the Doppler shifts on both sides become asymmetric according to the inner/outer asymmetry of $d\Psi/dR$, in the outward shifted configuration. These examples show the dependence of the rotation velocity on the gradients of surface function ($V_p \propto dR/d\Psi$) qualitatively.

The C^{6+} ion density profile in these discharges measured using the intensity of the charge exchange spectral line are shown in Figure 4.1.2. This density profile is the intensity profile divided by the neutral beam density profile integrated along the observation chord in vertical direction calculated with the method described on section 3.3. The range of $\rho > 0$ denotes the outside of the magnetic axis and the range of $\rho < 0$ denotes the inside, where $|\rho|$ is the averaged minor radius of magnetic

surfaces. The central electron and ion temperatures and the line averaged electron density in the center chord in the discharge with the configuration of $R_{ax}=92.1\text{cm}$ are $T_e(0)=540\text{eV}$, $T_i(0)=650\text{eV}$ and $n_e = 1.5 \times 10^{13}\text{cm}^{-3}$, respectively. Those in the discharge with the configuration of $R_{ax}=99.5\text{cm}$ are $T_e(0)=200\text{eV}$, $T_i(0)=140\text{eV}$ and $n_e = 1.7 \times 10^{13}\text{cm}^{-3}$ respectively. In this density region, the density profiles of the beam in plasmas are not sensitive to the electron densities as mentioned in the section 3.3. The inside/outside asymmetry of the density profile of C^{6+} ions in Figure 4.1.2(b) is much larger than the error in the beam attenuation calculation. The CVI intensity profiles after subtracting the background are shown in Figure 4.1.3.

The averaged minor radius ρ is determined by the profile fitting of measured ion temperature to the magnetic surfaces calculated with the finite- β 3-D equilibrium code VMEC[43] since the plasmas have the Shafranov shifts enhanced by beam parallel pressure[45]. Figure 4.1.4 shows this profile fitting for the discharge with $R_{ax}=92.1\text{cm}$ using PROCTR-MOD[44]. The magnetic surface calculated for the condition of $\beta=0.5\%$ gives better fit though the volume averaged β by the diamagnetic measurement is $\beta=0.2\%$.

4.2 Comparison with the Momentum Balance Equation

The reason of the inside/outside asymmetric density profile in the configuration of $R_{ax}=99.5\text{cm}$ can be explained as follows. Poloidal and toroidal rotation velocities V_p , V_t at the mid-plane ($Z=0$) should follow the momentum balance equation

$$V_p B_t(R) - V_t B_p(R) = E_R - \frac{dp_i(\rho)/dR}{e Z_i n_i(\rho)} \quad (4.1)$$

where B_t , B_p , p_i , Z_i and n_i are the toroidal and poloidal magnetic field, the C^{6+} ion pressure, the charge of the ion ($Z_i=6$) and the ion density respectively. Because of the damping of the toroidal flows in the outward shifted configurations of CHS[18], the poloidal rotation velocity is determined only by the radial electric field term and the pressure gradients term in this equation. This fact is confirmed by the comparison of the velocity on both sides as follows. Figure 4.2.1 shows the measured rotation velocity and the diamagnetic drift velocity calculated from the ion temperature and the density profile. The radial electric field E_R at the mid-plane calculated using Eq(4.1) without the toroidal rotation velocity term $V_t B_p$ is shown in Figure 4.2.2, and the electrostatic potential at the mid-plane shown in Figure 4.2.3 is the integral of this electric field. The dependence of calculated potential on the averaged minor radius ρ has inside/outside symmetry. Since the electrostatic potential is constant on the magnetic surfaces, this result means that the poloidal rotation velocity of C^{6+} is determined only by the gradient of surface function. This relation between inside and the outside of the magnetic surfaces can be expressed also in the form

$$\frac{V_p(\text{in})}{V_p(\text{out})} = \frac{\Delta R(\text{out}) B_t(\text{out})}{\Delta R(\text{in}) B_t(\text{in})} \quad (4.2)$$

where ΔR is the surface spacing. The magnetic field strength B_t calculated using Biot- Savart's law is shown in Figure 4.2.4.

4.3 Poloidal Flow Conservation

The poloidal flux across the mid-plane per unit toroidal angle integrated in the magnetic surfaces

$$\int_{\text{axis}}^R V_p \cdot n_i \cdot R \cdot dR$$

calculated from the measured rotation velocity and the C^{6+} density profile is shown in Figure 4.2.1. The dependence of this integration on the averaged minor radius ρ has inside/outside symmetry that indicates the poloidal flow conservation. This conservation condition on the inside and outside of the magnetic surfaces can be expressed also in the form

$$n_i(\text{in}) V_p(\text{in}) \Delta R(\text{in}) R(\text{in}) = n_i(\text{out}) V_p(\text{out}) \Delta R(\text{out}) R(\text{out}) \quad (4.3)$$

The relation (4.2) and (4.3) lead the relation

$$\frac{n_i(\text{in})}{n_i(\text{out})} = \frac{B_t(\text{in}) R(\text{out})}{B_t(\text{out}) R(\text{in})} \quad (4.4)$$

The asymmetry of the density profile of C^{6+} shown in Figure 4.1.2(b) is consistent with this relation therefore the symmetry of the potential calculated without the toroidal rotation term and the flow conservation in both side are obtained simultaneously. Of course this density asymmetry can exist only in impurity ions with low pressure, thus it indicates that the poloidal rotation of bulk ions will be damped by the toroidal viscosity.

Although these quantitative analysis of inside/outside asymmetry of poloidal flow is difficult in the inward shifted configurations because of the intense background radiation at the inside of the magnetic axis which cause the degradation of signal/noise ratio of spectrum after subtracting background spectrum, the C^{6+} density profile shown in Figure 4.1.2(a) suggests the poloidal rotation accompanying the inside/outside asymmetric

toroidal flow. This also can be expected from the weak damping of toroidal flow in the inward shifted configurations[18]. The measurement of inside/outside asymmetry of toroidal rotation velocity in the inward shifted configurations is planned in near future.

4.4 Parallel Force Balance in the Outward Shifted Configuration (Future Theme)

The toroidal flow for the incompressible flow conservation will have the velocity of $V_t \sim V_p (2\pi / \iota)$. The preliminary measurement of the inside/outside asymmetry of toroidal rotation(Appendix 1) shows that these velocity component do not exist in the outward shifted configuration. It also support the conclusion described above.

On the other hand, if the parallel pressure gradient due to the asymmetric density is balanced by the viscosity force or the friction force to some kinds of parallel flows, this flow should be detected. However, this kinds of flow have never been detected in present. The improvement of the accuracy to detect this flow is an important future theme.

Not only the density of impurity ions but also their temperature may become non-uniform on magnetic surface in order to make the uniform pressure, as considered in the models of MARFE[46]. If this uniformity of temperature is exist, the Shafranov shift of the temperature profile of the impurity ions measured with CXS will differ from the shifts of the profiles of other quantities. Recent soft X-ray measurements in CHS[47] shows that the both of the value of shafranov shifts obtained from CXS measurements and soft X-ray measurements agree with each other within the errors in the configuration with $R_{ax}=89.9\text{cm}$, 92.1cm , 94.9cm and 97.4cm [48]. However, the improvement of the accuracy of both measurements and the comparison of both measurements are important future themes.

4.5 Effect of Neutral and Impurity Flux from the Inner Wall

In the inward shifted configurations (limiter configurations) of CHS, the plasmas touch the inner wall of the vacuum vessel. And plasmas are still near to the wall in the outward shifted configurations (diverter configurations) though they are detached from the wall in these configurations. In the final of this chapter, some comments that state that the measured density profiles are not affected by thermal neutral flux and impurity flux from the inner wall are appropriate.

Although the intensity of the CVI spectral line is hardly affected by the poloidal non-uniformity of thermal neutral density as described in Section 3.2, components caused by the charge exchange with thermal neutrals may be partially included in the background radiation. The measured density profiles, however, are obtained only from the intensity of NB charge exchange spectral line after subtracting the background radiation, thus the effect of thermal neutral flux from the inner wall is eliminated.

The density profile of fully ionized carbon will not be affected by the impurity flux from the inner wall, though the inside/outside asymmetry of the density due to the flux may occur in the case of impurity ions in low ionization states. When the ionization mean free paths are short compared with the plasma dimension or the ionization times are short compared with the temperature relaxation time ($\tau_T = 3(2\pi)^{1/2} \pi \epsilon_0^2 M_Z m_i (T_Z/M_Z + T_i/m_i)^{3/2} / (n_i Z^2 e^4 \ln \Lambda)$), where M_Z and T_Z are the mass and the temperature of the impurity ions, and M_i, T_i, n_i are the mass, the temperature and the density of bulk ions, $\ln \Lambda$ is the Coulomb logarithm respectively. $\tau_T = 1.4 \mu \text{ sec}$ in the condition with $T_Z = T_i = 100 \text{ eV}$, $n_i = 10^{13} \text{ cm}^{-3}$ and $Z=6$), the density of the impurity will be toroidally and poloidally non-uniform. Figure 4.5.1 shows the electron impact ionization rates of carbon in the various ionization states. The

inside/outside asymmetric density profile due to the impurity flux from the inner wall will occur only in the case of low ionization states(CII,CIII), and will not occur in the case of highly or fully ionization states(CVI,CVII). The toroidal and poloidal uniformity of the background radiation discussed in section 3.2 is originated from this fact and this is the one of the reason to measure the fully ionized carbon(not incompletely ionized carbon, or lighter impurities). The fact that the inside/outside asymmetry of the density profile was observed in diverter configuration($R_{ax}=99.5\text{cm}$) and the symmetry of the density was observed in limiter configuration($R_{ax}=92.1\text{cm}$) also holds the absence of the effect of the impurity flux from the inner wall.

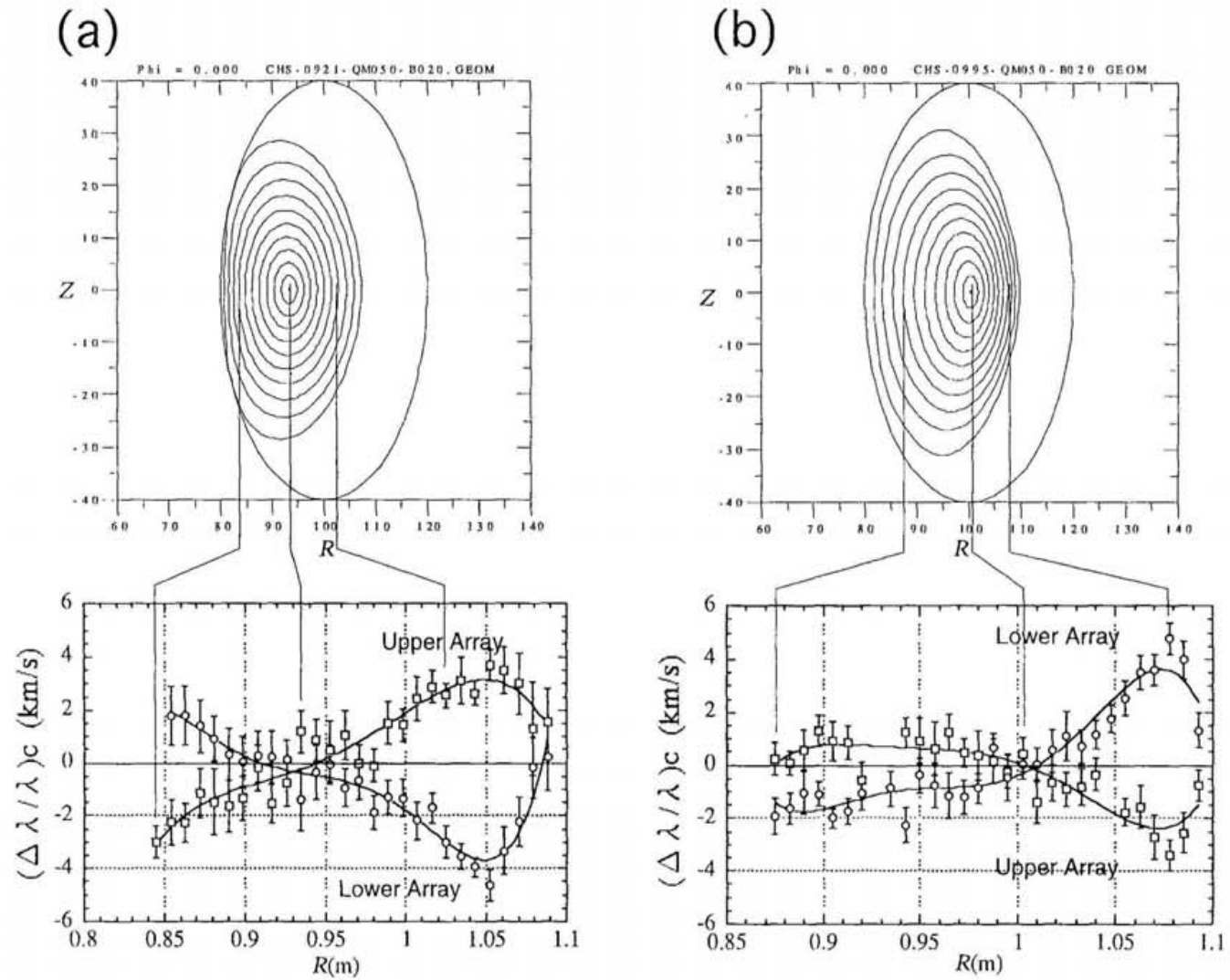


Figure 4.1.1. The Doppler shifts of CVI line ($\Delta n=8-7$, $\lambda=5292 \text{ \AA}$) at the vertically elongated section in the configurations with the major radius of the vacuum magnetic axis at (a) $R_{ax}=92.1$ cm and (b) $R_{ax}=99.5$ cm.

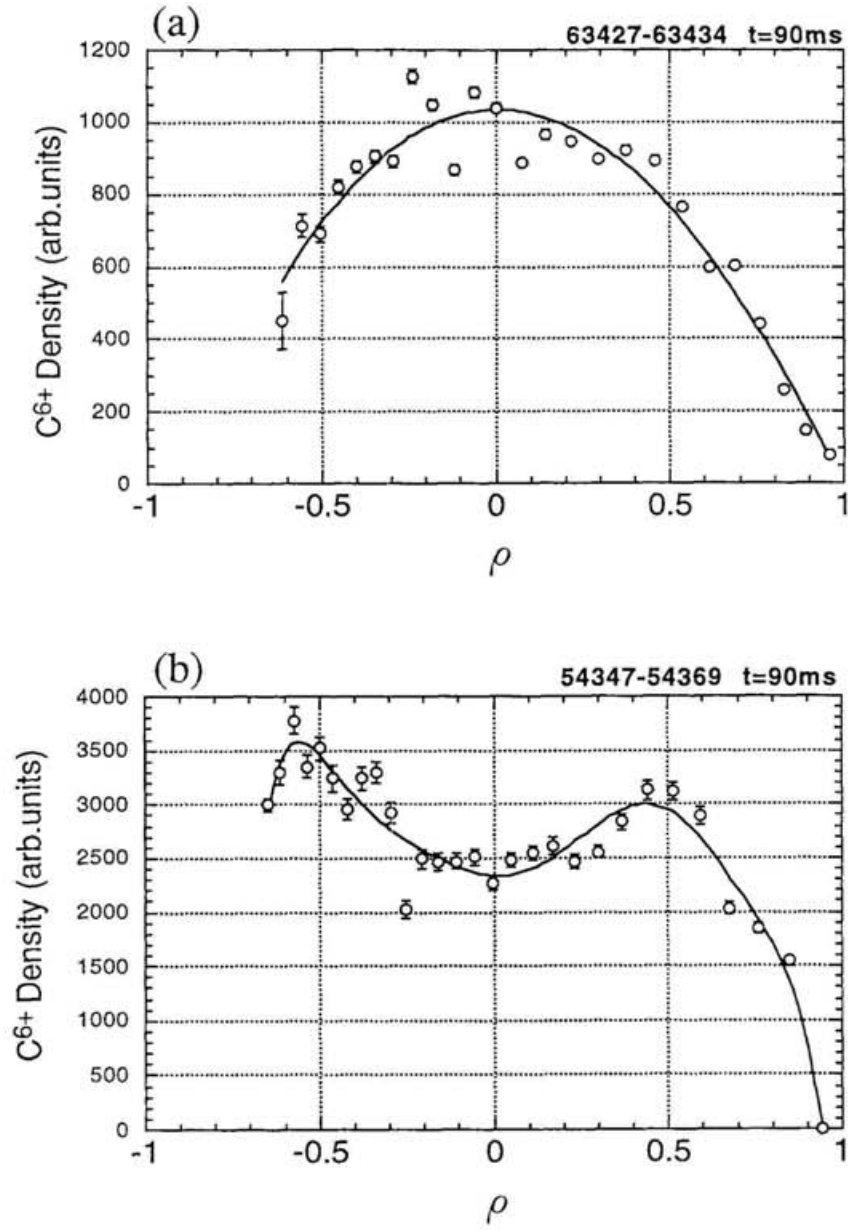


Figure 4.1.2. The C^{6+} ion density profile measured using the intensity of the charge exchange spectral line in the configurations of (a) $R_{ax}=92.1\text{cm}$ and (b) $R_{ax}=99.5\text{cm}$.

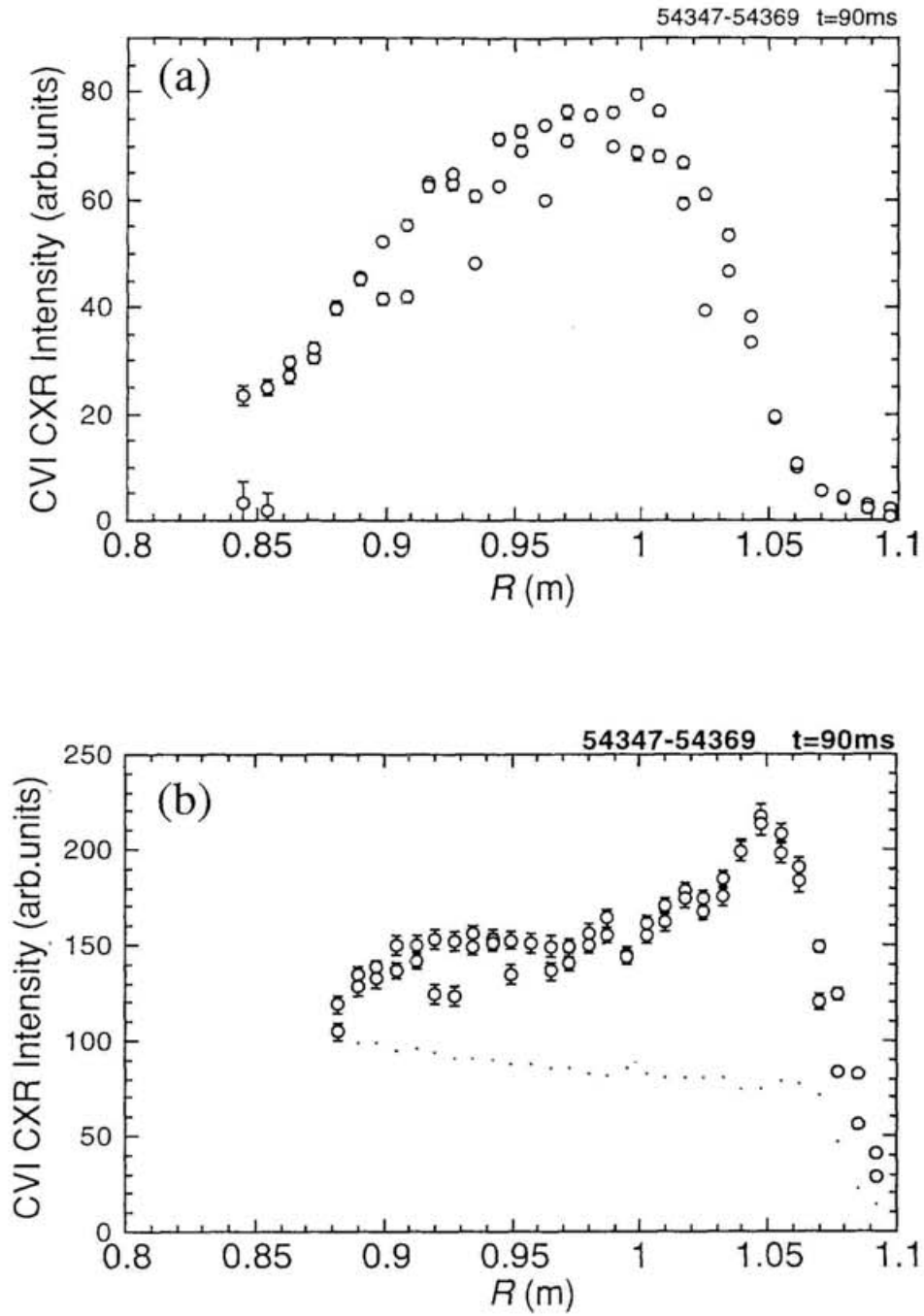


Figure 4.1.3 The intensity distributuion of charge exchange excited CVI line($\Delta n=8-7$, $\lambda=5292\text{\AA}$) in the configurations of (a) $R_{ax}=92.1\text{cm}$ and (b) $R_{ax}=99.5\text{cm}$.

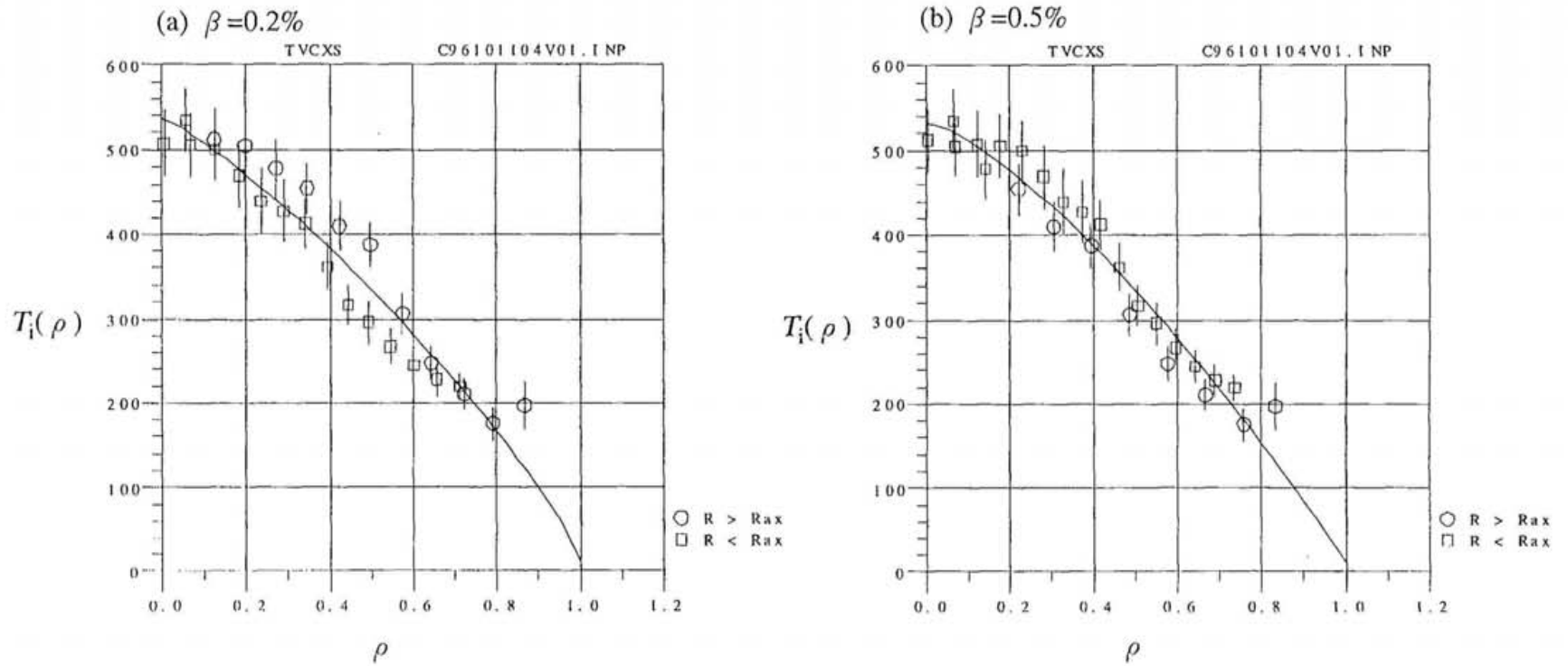


Figure 4.1.4 The example of the profile fitting of ion temperature T_i in inward shifted configurations.

○ denotes the outside of magnetic axis and □ denotes the inside of magnetic axis.

The magnetic surface calculated for the condition of $\beta = 0.5\%$ (b) gives better fit compared with that for $\beta = 0.2\%$ (a) though the volume averaged β by the diamagnetic measurement is $\beta = 0.2\%$.

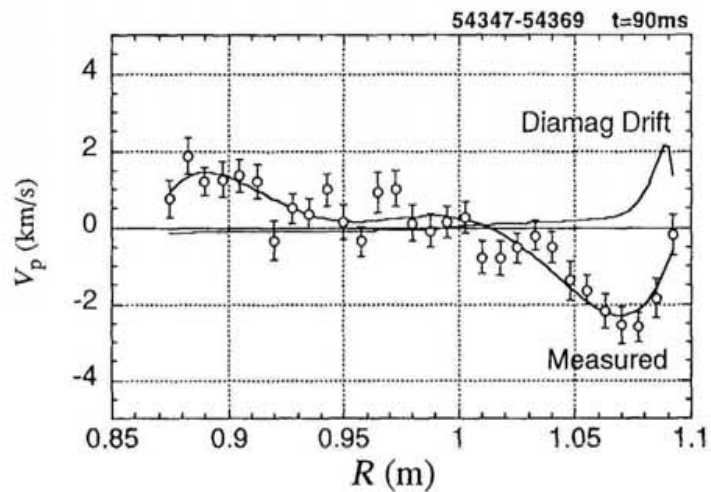


Figure 4.2.1 The measured rotation velocity and the diamagnetic drift velocity calculated from the ion temperature and the density profile E_R (V/cm) configurations of $R_{ax}=99.5$ cm.

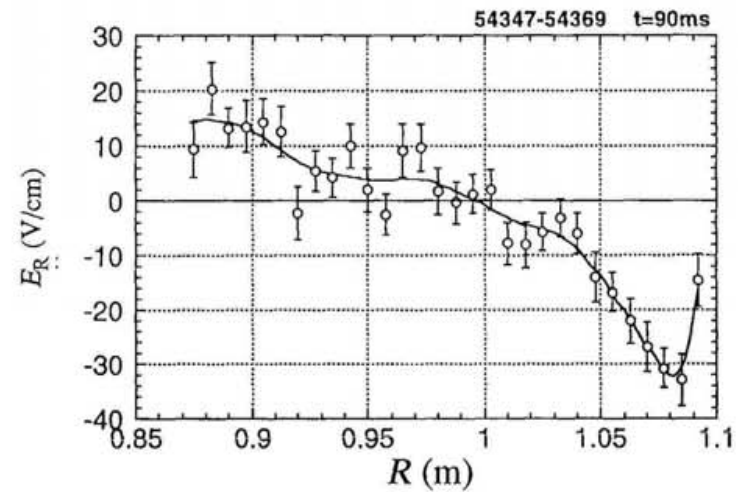


Figure 4.2.2 The radial electric field E_R at the mid-plane calculated using Eq(4.1) without the toroidal rotation velocity term $V_t B_p$ in the configurations of $R_{ax}=99.5$ cm.

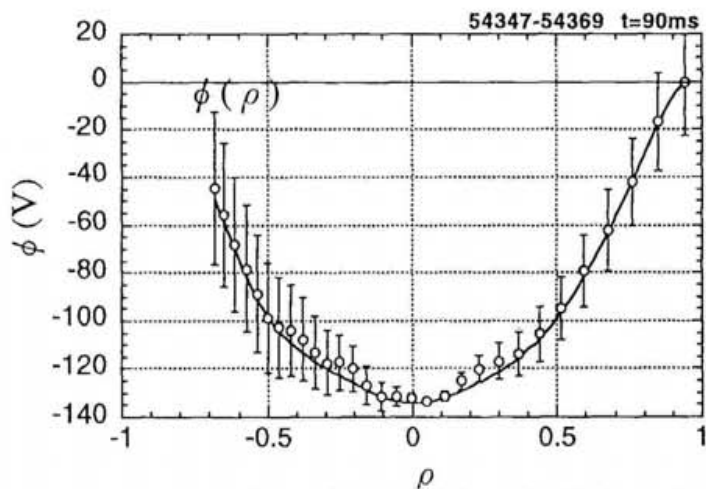


Figure 4.2.3 The electrostatic potential at the mid-plane derived by the electric field. The dependence of calculated potential on the averaged minor radius ρ has inside/outside symmetry.

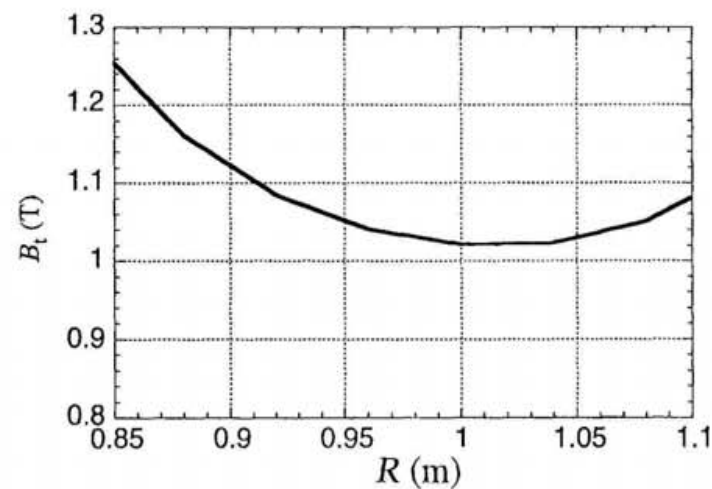


Figure 4.2.4 Magnetic field strength calculated using Biot- Savart's law

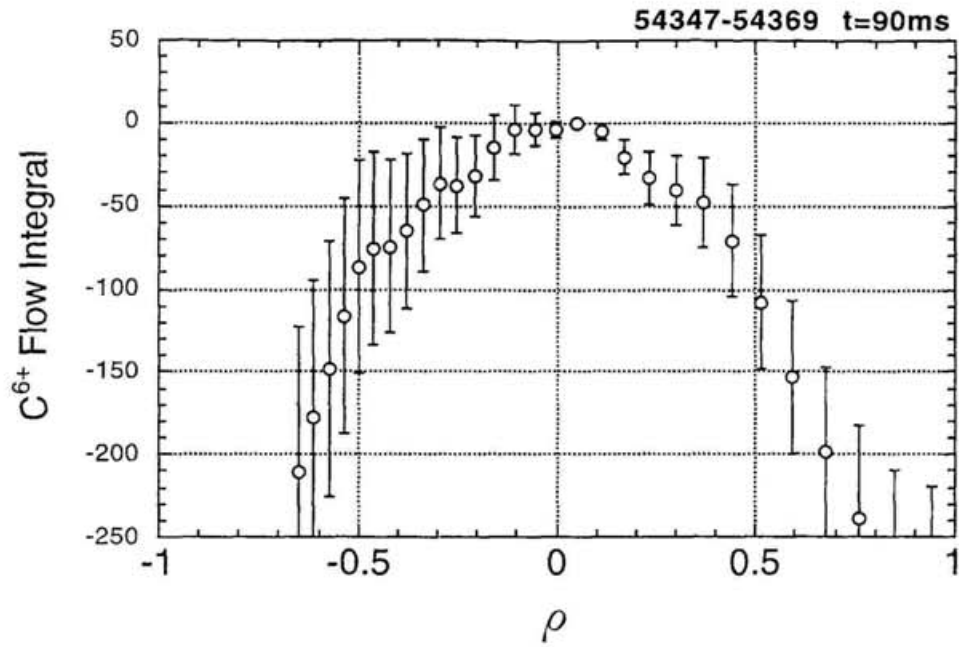


Figure 4.3.1 The poloidal flux across the mid-plane per unit toroidal angle integrated in the magnetic surfaces calculated from the measured rotation velocity and the C^{6+} density profile in the configuration of $R_{ax}=99.5\text{cm}$. The dependence on the averaged minor radius ρ has inside/outside symmetry that indicates the poloidal flow conservation.

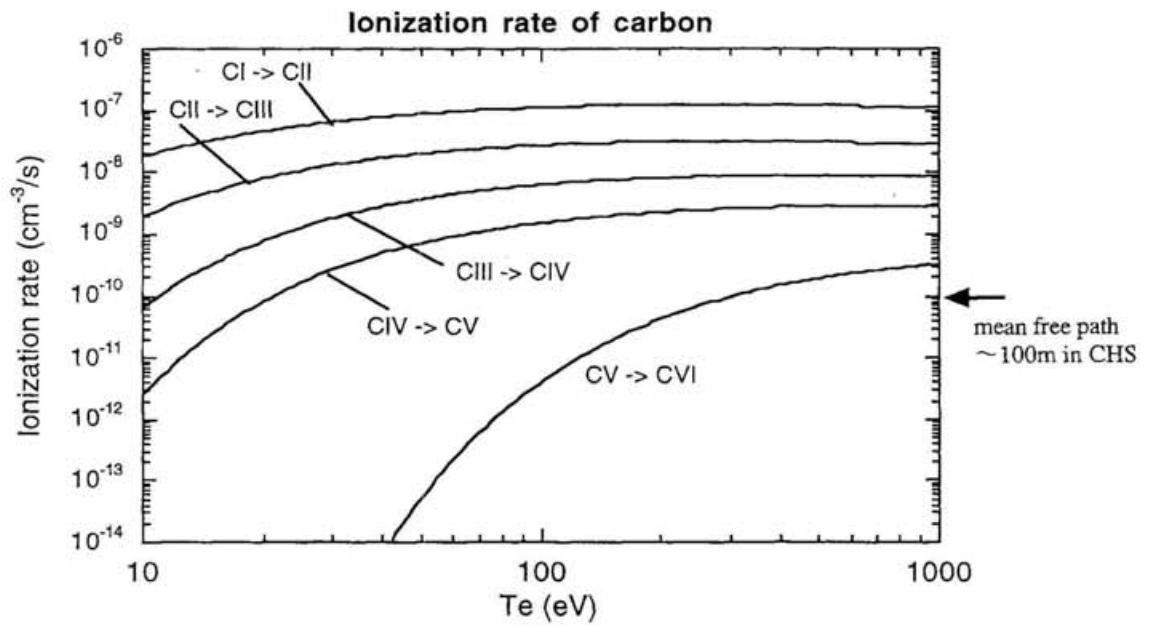


Figure 4.5.1 The electron impact ionization rates of carbon in the various ionization states.

Chapter 5

Conclusion

A new charge exchange spectroscopic system with fiber arrays viewing the neutral beam from upside and downside have been applied to detect the absolute values of poloidal rotation velocity in CHS experiments. The asymmetry of the poloidal rotation velocity and the density of fully ionized carbon ions on the inside and outside of the magnetic surfaces was successfully measured with the CVI line($\Delta n=8-7$, $\lambda=5290 \text{ \AA}$).

The preliminary measurement of plasmas with this system clarified several technical problems in multi-channel CXS. The most important problem was the apparent wavelength shifts caused by the spectral fine structure of hydrogen-like ions used in CXS. This shift introduces the errors of a few km/s in evaluating the poloidal rotation velocity and is not negligible. These fine structures are well described by the collisional l-mixing model and the correction can be made with ease. To subtract the cold component of the spectrum due to the background radiation, the reference channels looking off the neutral beam line is adopted. The intensity of the background radiation has toroidal periodicity, which is assumed in this method, since it is caused mainly by the electron impact ionization of hydrogen-like $A^{(Z-1)+}$ ions. To measure the density profiles of the fully ionized impurity ions, the initial beam density profile without attenuation was also measured in the torus using H_{α} originated from the beam. The calculated result of the beam attenuation shows that the plasma densities should be chosen to be low (with the line averaged density of $n_e < 2 \times 10^{13} \text{ cm}^{-3}$) to avoid the ambiguity of beam attenuation calculation and the degradation of signal level on the inside.

In the outward shifted configuration, the measured rotation velocity has strong inside/outside asymmetry corresponding to the asymmetry of the magnetic surface configuration. The electrostatic potential calculated with this velocity using the momentum balance equation without the toroidal rotation term is the

surface quantity because of the damping of the toroidal flows in this configuration. However, this fact conflicts to the incompressible poloidal flow conservation condition. The measured density of ions have a hollow profile and is higher on the inside of the magnetic surfaces compared with that on the outside. This inside/outside asymmetry of the density profile can be explained by the poloidal flow conservation on both sides. This phenomena observed in impurity ions with low pressure indicates that the poloidal rotation of bulk ions will be damped by the toroidal viscosity.

In the inward shifted configuration, the density has flat or a peaking profiles and the inside/outside asymmetry is not clear. Although the quantitative comparison of the electrostatic potential and the poloidal flow on both sides is difficult in the inward shifted configurations because of the intense background radiation at the inside of the magnetic axis which cause the degradation of signal/noise ratio of spectrum after subtracting background spectrum, this change in the density asymmetry is consistent to the past measurement of toroidal rotation damping and suggests the poloidal rotation accompanying the inside/outside asymmetric toroidal flow. Therefore the measurement of inside/outside asymmetry of toroidal rotation velocity is a interesting future theme.

This is the first observation of the asymmetry of the poloidal rotation velocity and the density of impurity ions on the inside and outside of the torus that demonstrates new need and feasibility to measure the quantities non-uniform on magnetic surfaces to study phenomena related to plasma rotations

References

- 1) B.B.Kadomtsev and O.P.Pogutse; Nucl.Fusion 11 (1971)67
- 2) H.Sanuki, J.Todoroki and T.Kamimura; Phys.Fluids B2 (1990)2155
K.Itoh, H.Sanuki, J.Todoroki,et.al; Phys.Fluids B3 (1991)1294
- 3) K.Itoh and S.-I.Itoh; Plasma Phys.Controlled Fusion 38 (1997)1
- 4) F.L.Hinton and R.D.Hazeltine; Rev.Mod.Phys.48 (1976)239
- 5) R.D.Hazeltine, E.P.Lee and M.N.Rosenbluth; Phys.Fluids 14 (1971)361
- 6) J.M.Green and N.K.Winsor; Phys.Fluids16 (1973)863
- 7) K.C.Shaing, R.D.Hazeltine and H.Sanuki; Phys.Fluids B4 (1992)404
K.C.Shaing,C.T.Hsu and P.J.Christenson;Plasma Phys.Control.Fusion 36 (1994)A75
- 8) A.B.Hassam and J.F.Drake; Phys.Fluids B5 (1993)4022
- 9) R.J.Groebner,K.H.Burrell,at.al.; Rev.Sci.Instrum. 61 (1990)2920
- 10) K.Ida, S.Hidekuma, Y.Miura, et.al.; Phys.Rev.Lett. 65 (1990)1364
- 11) A.R.Field,G.Fussmann,J.Hofmann, et.al.; Nucl.Fusion 32 (1992)1191
- 12) J.Kim, K.H.Burrell, P.Gohil, et al.;Phys.Rev.Lett. 72 (1994)2199
- 13) J.V.Hofmann,K.Ida,J.Geiger,et.al.; in Proc.21th European Conf.on Controlled
Fusion and Plasma Physics(Montpellier,1994) contributed papers, Part I,p.392
- 14) K.Kondo, H.Zushi, S.Nishimura, et.al.; Rev.Sci.Instrum. 59 (1988)1533
- 15) K.Ida,H.Yamada,et.al.;Phys.Fluids B3 (1991)515 andB4 (1992)1360
- 16) R.B.Howell,R.J.Fonck, et.al.;Rev.Sci.Instrum. 59 (1988)1521
- 17) K.Ida, S.Hidekuma, et.al.;Rev.Sci.Instrum. 60 (1989)867
- 18) K.Ida, H.Yamada, H.Iguchi, K.Itoh, and CHS Group; Phys.Rev.Lett. 67 (1991)58
- 19) K.Ida and N.Nakajima; Phys.Plasmas 4(1997)310
- 20) K.C.Shaing; Phys.Fluids 27 (1984)1567
- 21) D.E.Hastings, W.A.Houlberg and K.C.Shaing; Nucl.Fusion 25 (1985)445
- 22) K.C.Shaing, S.P.Hirshman and J.D.Callen; Phys.Fluids 29 (1986)521
- 23) H.Sanuki, K.Itoh, K.Ida and S.-I.Itoh; J.Phys.Soc.Japan 60 (1991)3698
H.Sanuki, K.Itoh, S.-I.Itoh; J.Phys.Soc.Japan 62 (1993)123
- 24) A.Fujisawa, H.Iguchi, S.Lee, T.P.Crowley, et al.;Phys.Plasmas 4(1997)1357
- 25) R.J.Groebner,K.H.Burrell and R.P.Seraydarian; Phys.Rev.Lett. 64 (1990)3015
- 26) R.C.Isler; Phys.Rev.Lett. 38 (1977)1359
- 27) R.J.Fonck, M.Finkenthal, R.J.Goldston, et.al.; Phys.Rev.Lett. 49 (1982)734
- 28) R.J.Groebner, N.H.Brooks, K.H.Burrell and L.Rottier;Appl.Phys.Lett. 43 (1983)920
- 29) R.J.Fonck, D.S.Darrow and K.P.Jaehnig; Phys.Rev. A29 (1984)3288

- 30) H.A.Bethe and E.E.Salpeter; Quantum Mechanics of One- and Two-Electron Atoms
(Plenum/Rosetta, New York, 1977)84
- 31) R.M.Pengelly and M.J.Seaton, MNRAS 127 (1964)165
- 32) W.J.Karzas and R.Latter; Astrophys.J.Suppl.Ser. 6(1961)167
- 33) S.Nishimura, K.Ida and CHS Group; to be published in Proc.of the 8th International
Toki Conference on Plasma Physics and Controlled Nuclear Fusion.
- 34) H.Ryufuku; Japan Atomic Energy Reserch Institute Report JAERI-M82-031(1982)
- 35) H.Tawara and W.Fritsch; Phys.Scripta T28 (1989)58
- 36) K.L.Bell, H.B.Gilbody, J.G.Hughes, et.al;
Culham Laboratory Report CLM-R216(1981)
- 37) R.Mewe; Astron&Astrophys. 20 (1972)215
- 38) C.Fleurier and J.Chapelle; Comput.Phys.Commun. 7(1973)200
- 39) C.Breton,C.de.Michelis and M.Mattioli; Euratom-CEA Report
EUR-CEA-FC-FC853(1976)
C.Breton,C.de.Michelis and M.Finkenthal and M.Mattioli; Euratom-CEA Report
EUR-CEA-FC-FC853(1978)
- 40) K.Ikeda, Y.Nagayama, T.Aota, et.al.; Phys.Rev.Lett. 78 (1997)3872
- 41) K.Ida, S.Nishimura, S.Takayama, et.al.; Ann Rep.of NIFS (1996)240
- 42) A.C.Rivere; Nucl.Fusion 11 (1971)363
- 43) S.P.Hirshman, W.van Rij and P.Merkel; Comput.Phys.Commun. 43 (1986)143
- 44) H.C.Howe; Oak Ridge National Laboratory Report ORNL/TM-11521(1990)
- 45) H.Yamada, K.Ida, H.Iguchi, S.Morita, et.al.; Nucl.Fusion 32 ,25(1992)
- 46) T.E.Stringer; in Proc.12th European Conf.on Controlled Fusion and Plasma
Physics(Budapest,1985) contributed papers, Part I,p.147
J.Neuhauser, W.Schneider, R.Wunderlich; Nucl.Fusion 26 (1986)1679
- 47) S.Ohdachi, S.Takagi, M.Takechi, K. Toi, et.al.; in 24th European Conference on
Controlled Fusion and Plasma Physics(1997)
- 48) S.Ohdachi; private communication.

Appendix1.

Measurements of the Asymmetry of Toroidal Rotation

In order to investigate the incompressible flow pattern in the inward shifted configurations with weak toroidal viscosity and to investigate the parallel force balance in the outward shifted configurations with strong toroidal viscosity, the new toroidal rotation measurement system to measure the asymmetry of toroidal rotation on the inside and outside of the torus was installed on CHS recently. The preliminary measurement result in the outward shifted configuration ($R_{ax}=97.4\text{cm}$) is presented here. Figure A.1 shows the schematic arrangement of the experiment. The specifications and the results of the calibrations of this system are shown in table A.1 and Figure A.2.

This measurement system views the charge exchange spectral line produced by NBI#1 via port '7L' and views the background radiation via port '3L' tangentially. Although the bidirectional observation of the spectral lines is not possible using these tangential viewing port, the detection of absolute value of rotation velocity can be done with the wave length calibration using the spectral lines observed from upside and downside in vertically viewing port(7U/7D). Of course, if there is the distortion of the rotation velocity profile caused by the interference lines and so on as described in Section3.1, this system itself cannot check it. Therefore the absence of interference lines should be checked by the poloidal rotation measurements system using bidirectional viewing.

To obtain the local value of toroidal rotation velocity, it need some kind of inverse transform from the chord integrated spectrum using the A^{Z+} density profile and beam density profile discussed in Chapter3 and Chapter4 since the beam diameter is comparable to the plasma dimension in the vertical elongated section. At the first step of the preliminary measurement, however, the comparison of the cases with reversed magnetic fields was done. The inside/outside asymmetric toroidal flow component for the compensation of the asymmetry of inside/outside poloidal flow will change it's direction when the

direction of poloidal flow is reversed by reversing the magnetic field, while the toroidal flow component due to the momentum injection by NBI will not change by reversing the magnetic field. Therefore the change of the wave length shifts corresponding to the direction of the magnetic fields will express the magnitude of the inside/outside asymmetric toroidal flow component.

Figure A.3 shows the toroidal rotation velocities observed in the cases of the helical magnetic fields with the direction of counter clock wise(CCW) and clock wise(CW). The major radius R shown here is defined as the major radius of the cross point of observation chord and the vertical elongated section.

The changes of the wave length shifts on the inside and outside of the magnetic axis are less than 1km/s. The poloidal rotation velocity in this discharge is shown in Figure A.4. It has the same magnitude as that in the discharge described in Chapter 4. Therefore the inside/outside asymmetric toroidal flow component is too small to compensate the asymmetry of poloidal flow as discussed in Chapter 4, thus this result also holds the conclusion about the asymmetry of the density profile caused by the toroidal viscosity.

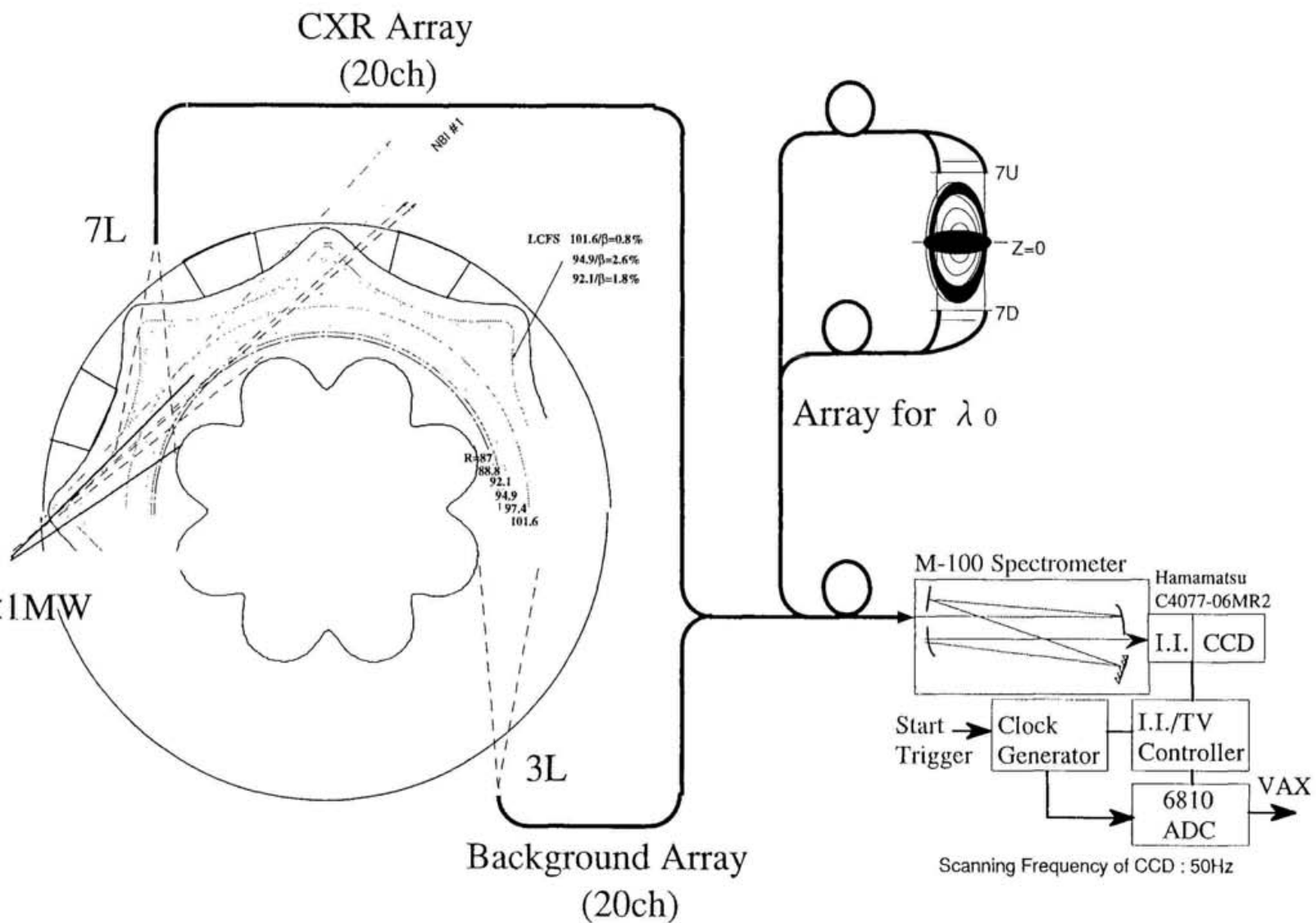


Figure A.1 Schematic Arrangement of Toroidal Rotation Measurement

Fiber Arrays

viewing chords 7mm ϕ parallel beam \times 16ch/array (fan-shaped arrangement)
fibers 125 μ m diam step-index quartz with 100 μ m core
(attenuation : 16dB/km)

Spectrometer (Jasco CT100-GD)

focus length 1000mm
grating 2160 l/mm
dispersion curve $\Delta \lambda$ ($\text{\AA}/\text{pixel}$) = $0.1285 + 6.79 \times 10^{-6} \times \lambda - 1.970 \times 10^{-9} \times \lambda^2$
where λ is the wavelength [\AA] (0.1 $\text{\AA}/\text{pixel}$ at $\lambda = 5000 \text{\AA}$)
instrumental width 9pixel

CCD detector with a image intensifier (Hamamatsu C4077-06MR2)

effective image size 8.8mm \times 6.6mm
I.I - CCD coupling fiber coupling
vertical scanning frequency 50kHz (CCIR)
nonlinearity correction curve
relative input (I_r) = $-0.00046 + 1.00 \times X - 1.3031 \times X^2 + 5.5175 \times X^3 - 8.5755 \times X^4 + 4.5505 \times X^5$
where X is the CCD output normalized by the saturation level (Figure 2.2)

Overall Sensitivity

radiant density = 1.7×10^{14} photon/cm²/ \AA /sr/s at the half of the saturation level in the condition of
 $\lambda = 6500 \text{\AA}$, gain = 6.5 (The detail dependence on the condition are shown in Figure A.2)

ADC(Lecroy 6810)&Clock Generator

sampling pixel 256 \times 243 (H \times V)
accuracy 12bit
sampling clock 5MHz
frame/shot 8

Table A.1 Specifications of the equipments
in the toroidal rotation measurement system

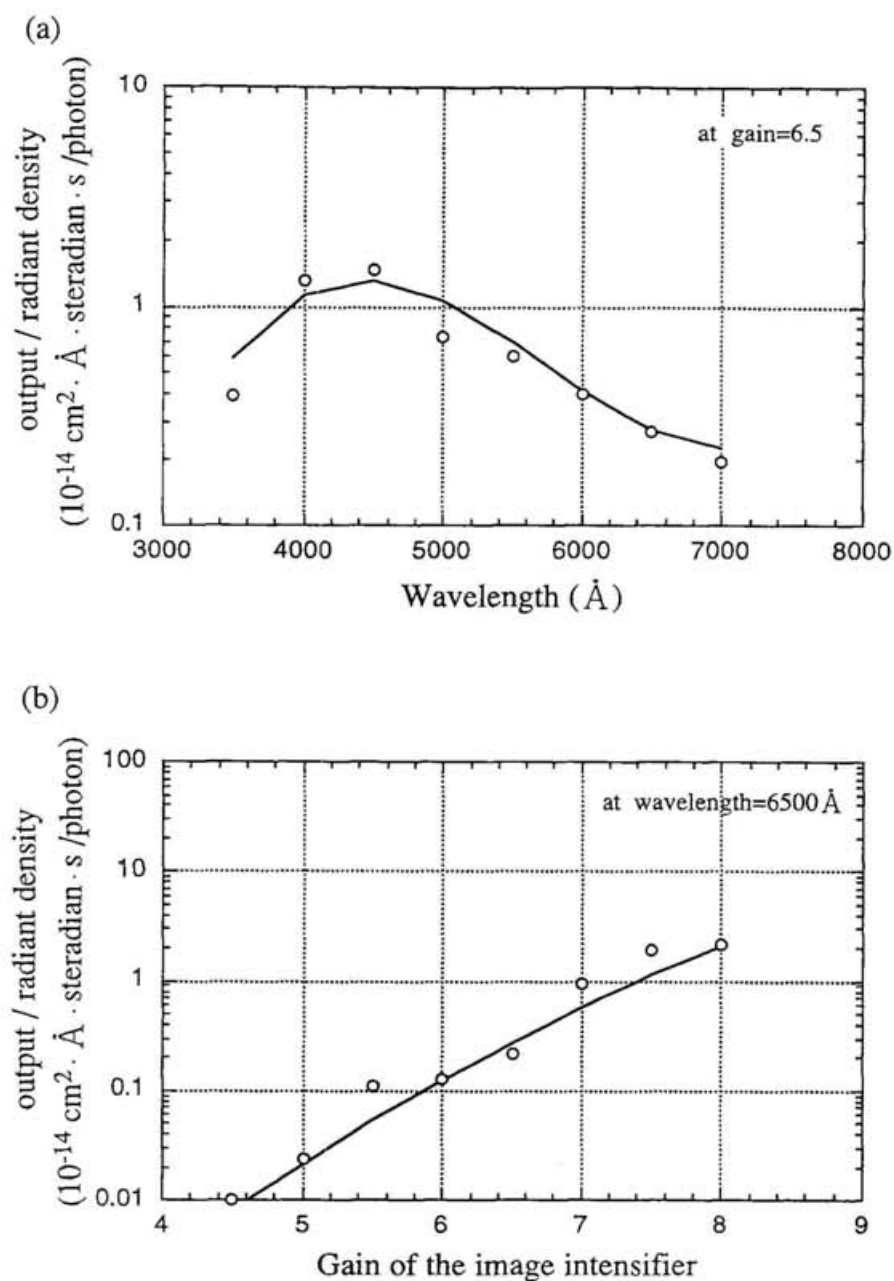


Figure A.2 The dependence of the absolute sensitivity on the wavelength(a) and the gain (accelerating voltage) of image intensifier(b). The definition of the output signal level of the system is described in Chapter 2.

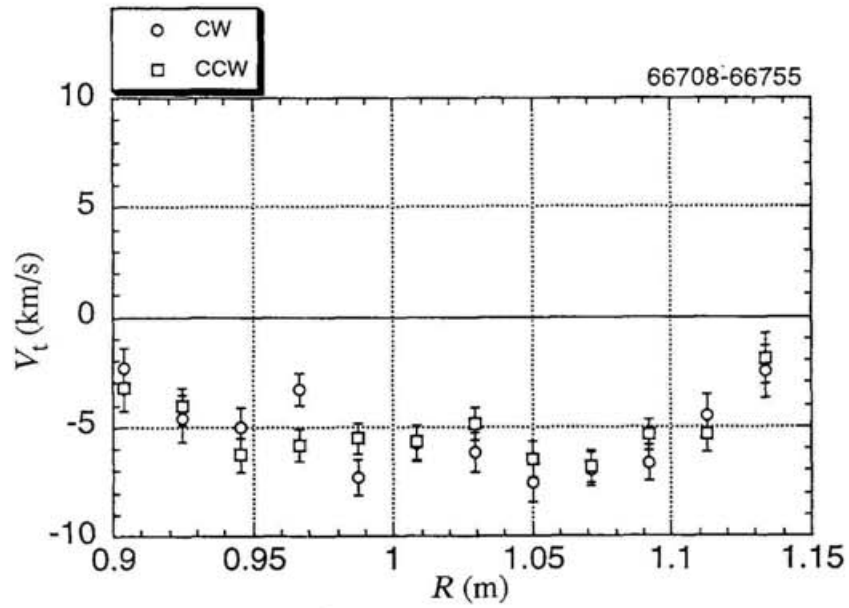


Figure A.3 The comparison of toroidal rotation velocities in the cases with reversed helical magnetic fields(CCW/CW).

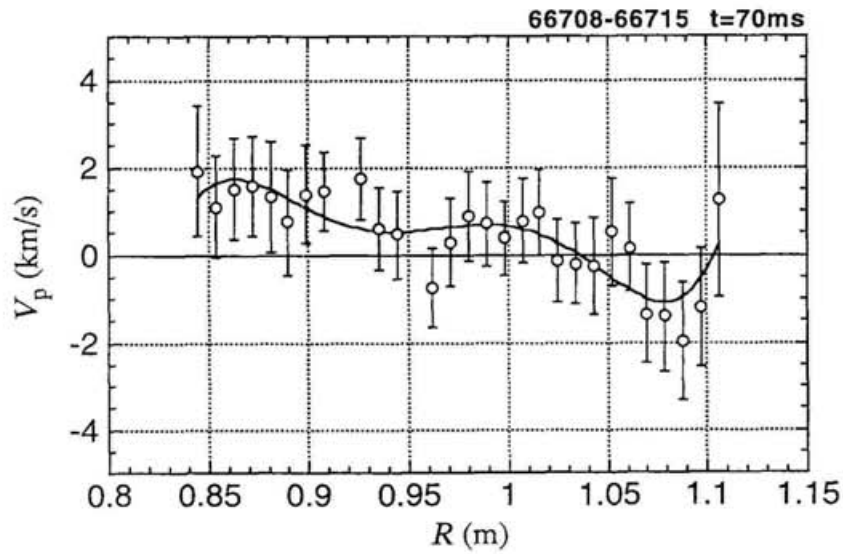


Figure A.4 The poloidal rotation velocity in this discharge.